AIAA Science and Technology Forum and Exposition, 23-27 January 2023, National Harbor, Maryland

A Computational Study of Plume Modeling For Space Launch System Abort Scenarios

Jonathan Boustani[1*], Michael P. Applebaum[1†], William M. Eppard[1‡],
Thomas B. Steva[2§], Leslie Hall[1¶]

[1]*Mclaurin Aerospace, Jacobs ESSCA Group, Huntsville, AL, 35802*

[2]*NASA Marshall Space Flight Center, Huntsville, AL 35808*

A series of viscous CFD simulations depicting Space Launch System (SLS) post Mode-1 abort scenarios are conducted and analyzed. The primary purpose of these simulations is to study the effect of launch abort vehicle attitude control motor (ACM) and abort motor (AM) plume modeling fidelity on the drag of the aborted core stage. The simulations are first conducted with a fully-coupled, multi-species and chemically reacting model for the freestream gases and the solid rocket abort motor combustion products. Following this, equivalent species are created for the ACM and AM exhaust gases. These equivalent species aim to provide near the same results for core stage drag as the chemically reacting model at a significantly lower computational cost. Finally, the exhaust gases are modeled as calorically perfect air. It was concluded that under most scenarios, both the equivalent species and the perfect air models predict the drag of the aborted core stage sufficiently close to that predicted by the chemically reacting simulations. In these cases, the flow and geometry conditions did not induce significant changes in the composition of the 'true' exhaust gas via afterburning of the combustion products. For cases where this was not the case, the properties of the essentially frozen equivalent species and perfect air models deviated from the true mixture, yielding unsatisfactory results. Finally, the accuracy improvements by using the chemically reacting model are weighed against the significant increase in associated computational costs. It was found that the simplified exhaust gas models are at least 4 times less expensive than the chemically reacting model. This may justify the judicious use of these simple models in future work.

I. Introduction

During crewed missions of NASA's Space Launch System (SLS), astronauts will ride aboard the Orion Multi-Purpose Crew Vehicle (MPCV). In order to protect these astronauts during abort scenarios, the MPCV is shrouded by a launch abort system (LAS) containing three sets of solid rocket motors (SRM) along a tower atop the crew module. Collectively, this is referred to as the launch abort vehicle (LAV). During a pad or launch abort scenario, the abort motor (AM), near the top of the LAV tower would fire for approximately three seconds, generating over 400,000 lbf of thrust, with the intention to quickly distance the crew in the MPCV from the core stage of SLS. One of the primary concerns during an in-flight abort, however, is that the aborted core stage could catch up to and impact the MPCV. Thus, the accurate prediction of drag on the aborted core stage during these scenarios is of the upmost importance.

The core stage drag is characterized by several factors, including: (1) the freestream Mach number and dynamic pressure, (2) the distance from the departing LAV to the leading edge of the aborted core stage, and (3) the interaction of the AM and attitude control motor (ACM) plumes with the freestream. We note that

*Aerospace Engineer, AIAA Member, jonathan.boustani@mclaurin.aero.
†Senior Aerospace Engineer
‡Senior Aerospace Engineer
§Aerodynamics Team Lead, Aerosciences Branch
¶Director of Engineering, AIAA Member

the most conservative estimate of the axial force coefficient on the aborted core stage, CA, is 0, though this is an extremely limiting assumption. Less conservative estimates for core stage CA were obtained after NASA tasked the authors with the generation of a database that produces the axial drag on the core stage following a Mode-1 abort scenario, or, within the first $120s$ of flight, as a function of the freestream conditions, vehicle orientation, and LAV position upstream of the aborted core stage.

Though the details of the database generation are not discussed here, a brief overview is provided in the following paragraph in order to situate the contents of this paper. The database provided to NASA by the authors consists of approximately 400 viscous computational fluid dynamics (CFD) simulations using the loci/CHEM unstructured solver.[1,2] All of the database simulations that considered the LAV upstream of the aborted core stage were 'unpowered'. That is, while the effect of geometric blockage from the LAV was included, the effect of AM and ACM plumes on the core stage drag were not included. This was deemed to be a conservative decision as the plumes were thought to raise CA relative to the unpowered simulations due to impingement on the core stage.

In order to evaluate this assumption, the authors employed a 15-species, 30-reaction exhaust gas model provided to the authors by Peter McCloud from NASA Johnson Space Center (JSC) to conduct a selection of powered 'check cases' from the database. These powered check cases were also used as an opportunity to study the fidelity required to model the exhaust gas and its chemical reactions. During the authors' prior efforts modeling rocket motor exhaust plumes for launch vehicle applications,[3] it was found that in many cases, the bulk properties and behavior of a multi-species, reacting gas mixture could be captured using a single 'equivalent' species that represents the entire mixture, or even perfect air – depending on the quantities of interest and the range of relevant length scales.

The comparison of these powered check cases to the unpowered database and the comparison between the different exhaust gas models are the topics of the present work. The results of this study will guide the development of databases for additional SLS configurations as the present work considers only the Block 1 configuration. The motivation to study the exhaust gas modeling is driven by the difficulties that are associated with the fully-coupled chemically reacting gas model. This not only includes requiring significantly more information about the composition of the exhaust gas, but from the numerical side, reacting gas models typically increase linear system stiffness and size, both of which contribute to a significant increase in the wall-time and computational resources required to conduct CFD simulations. This often makes the approach untenable for database generation where a large number of runs are needed. Since the current database is generated using an unpowered AM and ACM, if a significantly less-expensive computational approach is able to predict the aborted core stage drag with sufficient accuracy, future databases can be constructed with less uncertainty due to modeling error while simultaneously lowering the level of conservatism built into in the database. Beyond this, many launch vehicle applications (ascent, booster separation, stage separation), include motor plumes where the findings of this work may also be applicable.

The current paper proceeds as follows: Sec. II details the setup of the CFD simulations and the test matrix summarizing the geometric and flow conditions for the powered check cases. Sec. III summarizes the numerical methodologies used to conduct the CFD simulations and an overview of each of the exhaust gas models used. Sec. IV presents extended analyses that focus on the effect that the different exhaust gas models have on the aborted core stage drag via surface pressure analysis and line loads analysis. Finally, the computational costs of each method are compared against each other on a model problem in Sec. V before conclusions are stated in Sec. VI.

II. Problem Setup

A. Geometry

The outer mold line (OML) used in the current work is derived from the SLS Block 1 crewed configuration. This is shown in Fig. 1. The LAV is shown in grey, the relevant drag surfaces on the core stage and boosters are shown in blue, and the rest of the geometry is shown in orange. All simulations are considered at an angle-of-attack and side-slip angle of 0°.

Also shown in Fig. 1 is a dimensional characteristic length of the SLS core stage labeled $L_{ref.}$ and the dimensional distance from the leading edge of the SLS core stage to the aft end of the MPCV is labled as Δx. In this work, the dimensionless LAV offset, $\Delta x/L_{ref.}$, is varied from 0.5, 1.5, and 2.5 in order to determine a relationship between the LAV offset distance and the core stage drag. Fig. 2a shows a schematic of the LAV that highlights the location of the ACM and AM nozzles.

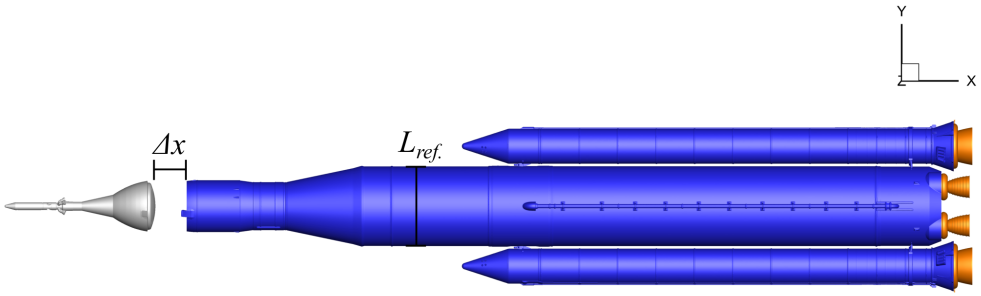

Figure 1: Schematic of the SLS Block 1 geometry used in the current work with the LAV offset.

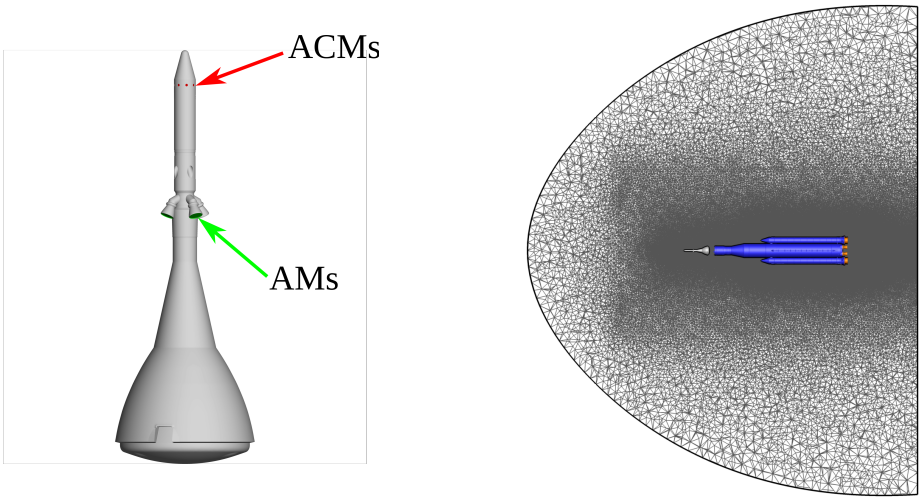

Figure 2: (a) Schematic of the LAV with the ACMs and AMs nozzle exits colored and (b) the unstructured volume mesh and domain boundaries shown on the $x-y$ plane.

B. CFD Simulation Setup

The above geometry is triangulated and placed in the center of a hemispherical domain, and a hybrid unstructured volume mesh is generated between the surface triangulation and the domain boundaries (see Fig. 2b) using Mississippi State's AFLR3 mesher.[4,5] Cells are clustered in the volume near the body and downstream of the vehicle. This process yielded a volume domain of approximately 270 million cells for all cases.

In the development of the unpowered post Mode-1 abort database, the authors observed that the Mach numbers $M = 0.7$ and $M = 3.0$ displayed the lowest drag on the core stage when downstream of the LAV. In addition, the Orion LAV AM thrust conditions were provided to the authors from NASA JSC in the form of a lower, nominal, and upper bound. Thus, the CFD run matrix used to guide the powered check cases considers the freestream Mach numbers of $M = 0.7$ and $M = 3.0$ and a relevant 'low-' and a 'high-thrust' condition for the AM that bounds the provided data. For all simulations, the ACM thrust is held at a constant value with the nozzles in a 'null' configuration, inducing no aerodynamic moments on the LAV. The full CFD run matrix, including the dimensionless LAV offset parameter, $\Delta x/L_{ref.}$, is summarized in Table 1.

In order to overcome the range of disparate length scales between the AM and ACM combustion chambers ($\mathcal{O}(10^{-1}m)$) and the length of the vehicle ($\mathcal{O}(10^{2}m)$), and to assist in the development of simplified exhaust gas models, a series of precursor simulations that include only the AM and ACM internals are conducted using the chemically reacting exhaust gas model (see Figs. 3 and 4, respectively). Stagnation pressures and temperatures that were provided to the authors by NASA JSC are specified in the combustion chamber, and

Table 1: CFD Run Matrix

$\Delta x/L_{ref.}$	Mach Number	AM Thrust Level
0.5	0.7, 3.0	Low, High
1.5	3.0	Low, High
2.5	3.0	Low, High

supersonic outlet boundary conditions are specified at the nozzle outflow planes. This boundary condition was chosen after ensuring that the nozzles were not over-expanded for all cases. All other nozzle surfaces are treated as adiabatic, no-slip walls.

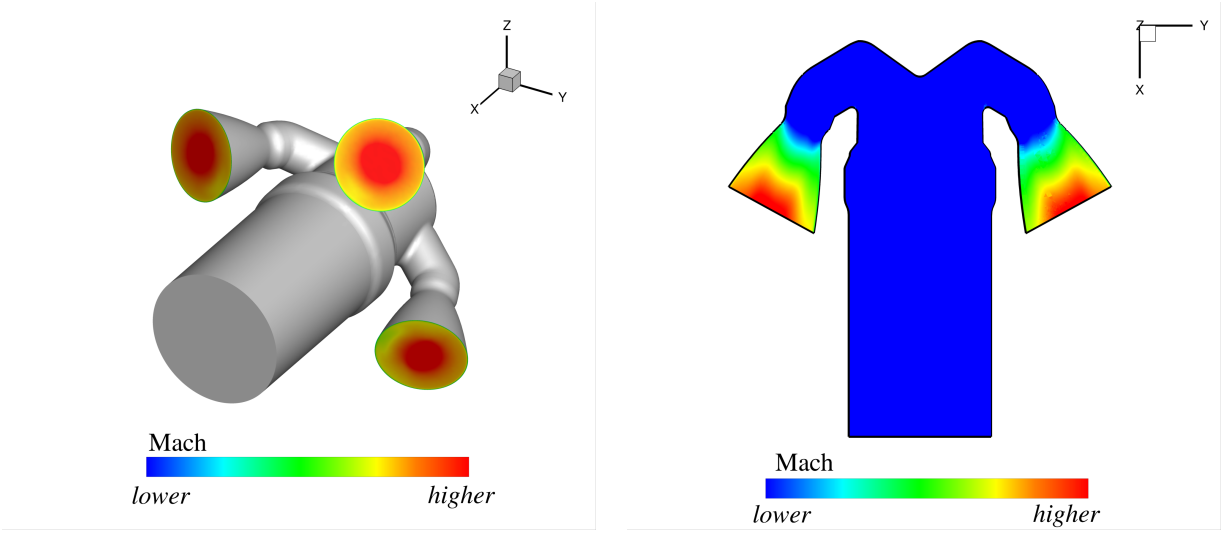

(a) (b)

Figure 3: (a) Perspective and (b) cut-plane views of saturated pseudocolor contours of Mach number shown for the precursor AM combustion chamber simulation conducted with the 15-species, 30-reaction chemical model.

The state variables as well as the species mass fractions obtained at the nozzle *outflow* planes from these precursor simulations are used to define an *inflow* plane in the case of the the full-scale simulations involving chemically reacting exhaust gases. For the full-scale simulations involving simplified exhaust gas models, the state variables and species mass fractions at the outflow planes are first used to define a single species that captures the specific heat and molecular weight of the 'true' exhaust mixture and engine thrust using the procedures outlined in Sec. III. Then, that single species is prescribed at the nozzle outlets as the inflow plane for the full-scale simulations. Note that no cases consider the solid rocket boosters (SRB) or core stage engines (CSE) firing. It is the experience of the authors that SRB and CSE plume effects near the aft end of the vehicle have little to no effect on forebody forces and moments.

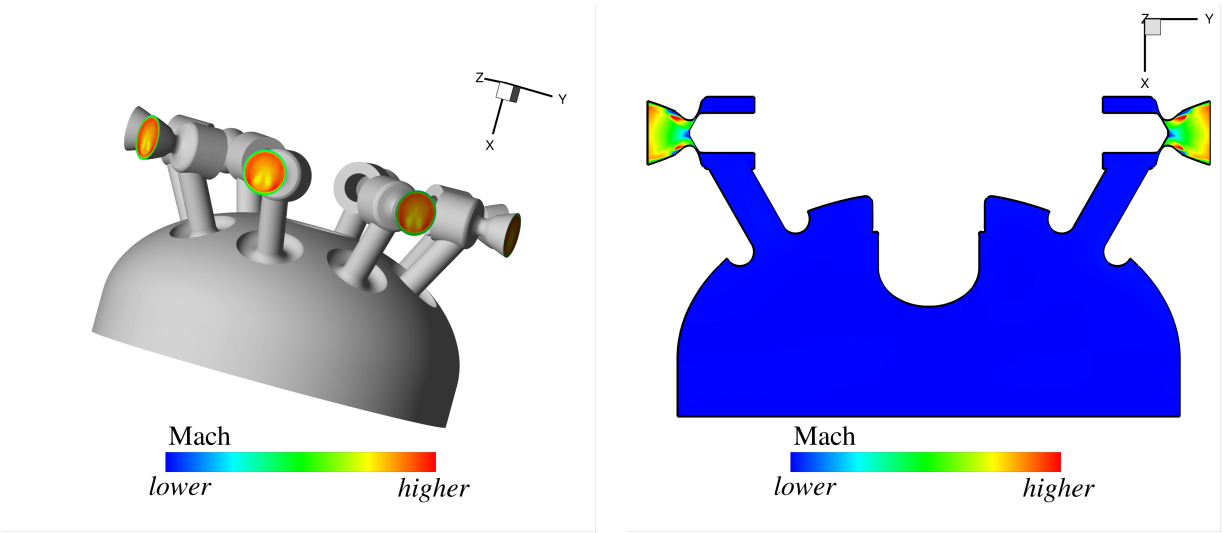

(a) (b)

Figure 4: (a) Perspective and (b) cut-plane views of saturated pseudocolor contours of Mach number shown for the precursor ACM combustion chamber simulation conducted with the 15-species, 30-reaction chemical model.

III. Methodology

A. CFD Solver

All simulations were performed using steady-state time integration within Mississippi State's loci/CHEM viscous Navier-Stokes solver.[1,2] In order to handle the large discontinuities in the supersonic flow field, loci/CHEM's high-speed module is used. In this module, the convective terms are discretized with a blended Roe-HLLE scheme – the latter, more dissipative scheme activating in and just downstream of regions with strong pressure gradients in the flow field. The thresholded Venkatakrishnan flux limiter[6] is also employed to aid in the computation of flux derivatives. The flowfield turbulence is modeled with Wilcox's 2008 $k-\omega$ model[7] using Wilcox's compressibility correction.[8] All surfaces are treated as no-slip, adiabatic walls unless otherwise specified.

B. Exhaust Gas Modeling

1. Multi-Species Model with Finite Rate Chemistry

The ACM and AM exhaust gases are first modeled with a 15-species, 30-reaction chemical kinetic model provided to the authors by Peter McCloud at NASA Johnson Space Center where it was derived from work by Niu *et al.*[9] The 15 species in the model are as follows: CO_2, CO, Cl_2, Cl, H_2O, H_2, HCl, HO_2, H, N_2, NO, N, O_2, OH, O, and 30 of their associated reactions are also included. An additional continuity equation must be solved for each of the listed species, significantly increasing the memory requirements and resources required for the CFD simulations. The increased cost of this model compared to the following models will be quantitatively studied in Sec. V.

2. Equivalent Single-Species Model

Given the primitive state and composition of a gas mixture at a specific location, an 'equivalent' single species that matches the mass-averaged quantities of the 'real' mixture of gases can be defined. In this work, this location is the exit plane of the AM and ACM nozzles. The state and composition of the exhaust gases at the nozzle exits is determined by the aforementioned chemically reacting precursor CFD simulations of the AM and ACM combustion chambers (see Sec. II). Note that a different equivalent species is defined for each combination of chamber conditions and freestream Mach number as the composition of the exhaust

mixture at the nozzle exits varies with the conditions, thus simulations at different motor and freestream conditions have a slightly different equivalent species for the AM and ACM exhaust gases.

The construction of the equivalent species starts by area-averaging the mass fractions of the different species at the nozzle exits. Following this, given the individual species gas constants and the gas constant of the exhaust mixture at the nozzle exit, $R_{mix.}$, the gas constant of the single equivalent species, $R_{eqv.}$, can be defined by

$$R_{eqv.} = R_{mix.} = \sum_{i=1}^{N_{species}} \left(\frac{\rho_i}{\rho_{mix.}} \right) \Bigg|_{exit} R_i, \tag{1}$$

where ρ_i is the density of the i^{th} species in the mixture containing $N_{species}$ different species, $\rho_{mix.}$ is the density of the mixture, and R_i is the gas constant of the ith species. The molecular weight of the equivalent species, $M_{eqv.}$, can then be computed in the usual way,

$$M_{eqv.} = \frac{R_{univ.}}{R_{eqv.}}, \tag{2}$$

where $R_{univ.}$ is the universal gas constant. Following this, the pressure and velocity of the equivalent species at the nozzle exits are set to match those of the 'true' reacting mixture at the exits. This guarantees that the motor thrust is the same for the chemically reacting and equivalent species cases. The temperature can then be 'floated' using the equivalent species gas constant and the equation of state.

At this point, the single equivalent species would properly represent the mass and momentum of the 'true' exhaust gas mixture – matching the important quantity of motor thrust – but the thermodynamic response of the equivalent species, and thus, the energy of the exhaust gas mixture, has not yet been represented. Caloric imperfections in the exhaust gas mixture may become significant during the rapid expansion of the exhaust in the form of large plumes emanating from the AM and ACM nozzles. This expansion causes the gas to rapidly cool and the ratio of specific heats, γ, to decrease. To capture this, the specific heats can be expressed as a function of the local gas temperature.

Using the usual mass-averaging techniques for a mixture of gases, the specific heat at constant pressure for the single equivalent species, $c_{p_{eqv.}}$, can be expressed by

$$c_{p_{eqv.}}(T) = \sum_{i=1}^{N_{species}} \left(\frac{\rho_i}{\rho_{mix.}} \right) \Bigg|_{exit} c_{p_i}(T), \tag{3}$$

where $c_{p_i}(T)$ is the specific heat at constant pressure for the ith species at a local gas temperature of T. The species specific heat at constant pressure is given by a Laurent polynomial of degree 4 and order -2 that is of the form

$$\frac{c_{p_i}(T)}{R_{univ.}} = a_{1_i} T^{-2} + a_{2_i} T^{-1} + a_{3_i} T^0 + a_{4_i} T^1 + a_{5_i} T^2 + a_{6_i} T^3 + a_{7_i} T^4. \tag{4}$$

The coefficients $a_{1_i} - a_{7_i}$ are provided by McBride *et al.*,[10] where a least-squares fit is used to represent the thermodynamic response of the real gas 'i' that is originally provided by experimental data. Thus, by combining Eqs. (3) and (4), we can obtain mass-averaged coefficients, and thus, a mass-averaged specific heat at a constant pressure can be found for the single equivalent species. The result of this is plotted for the $M = 0.7$ freestream case with low-thrust AM and null ACM along with the specific heat and γ for the full mixture exhaust gas in Figs. 5a and 5b. A similar process can be conducted for enthalpy, entropy, and transport properties.[10]

One major short-coming of using a single equivalent species, however, is that any further chemical reactions that may occur due to significant cooling or heating of the gas (*e.g.*, via convection of the exhaust gases into a cool freestream or afterburning of the combustion products), would not be captured as the construction of the single species essentially 'freezes' the chemical composition of the true gas mixture at a point in time and space. In prior works,[3] it was found that using a calorically-imperfect equivalent species to model the plume exhaust gases emanating from a rocket engine provided similar pressures along the nozzle centerline compared to the same simulation considering chemical reactions. This held true for a few hundred nozzle exit widths downstream.[3] A primary motivation for the current work, however, is that while the ratio of specific heats changed with the cooling and expansion of the plume in these previous simulations, the

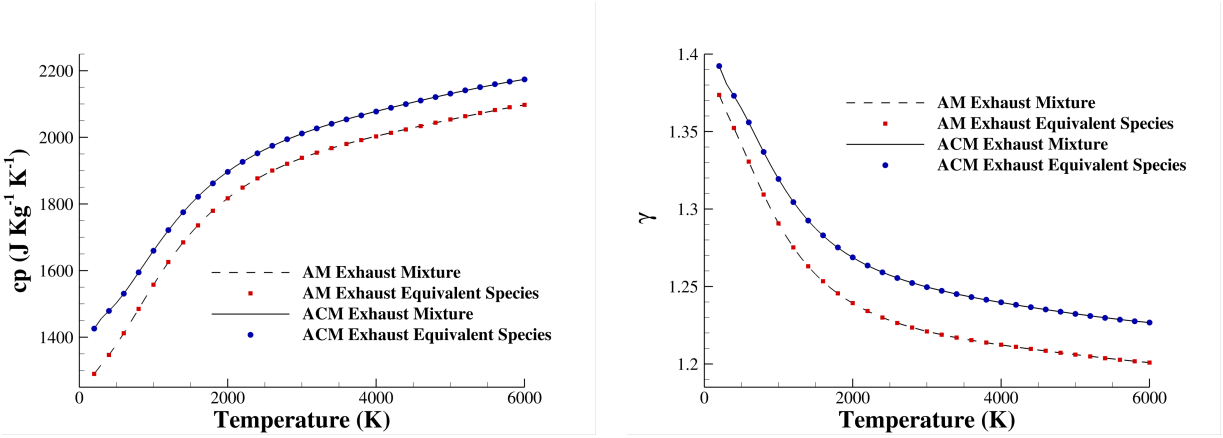

(a) (b)

Figure 5: (a) The specific heat at constant pressure and (b) ratio of specific heats for the AM and ACM exhaust gas mixtures as predicted by fully-chemically reacting simulations and by defining an equivalent species at the nozzle exits.

composition of the exhaust gas did not change significantly. Thus, the acceptable bounds for the application of the single equivalent species model and its deficiencies were not studied in detail. The current paper will continue the study from the prior works by investigating the effect of a growing disagreement between the composition of the equivalent species and the 'true' mixture on the prediction of aerodynamic loads.

3. Calorically Perfect Air Model

The most simple and widely-available exhaust gas model is that of calorically perfect air. In the present work, air is defined as a single species gas with molecular weight $M_{air} = 28.89 kg/mol$ and $n_{air} = 2.5$ that together, in addition to the ideal gas law, fully define the thermodynamic properties of the gas with the following relations:

$$n_{air} = \frac{c_{p_{air}}}{c_{p_{air}} - c_{v_{air}}} \tag{5}$$

and

$$c_{p_{air}} = c_{v_{air}} + R_{air} = c_{v_{air}} + \frac{R_{univ.}}{M_{air}}. \tag{6}$$

Due to its simplicity, this model has a variety of short-comings, most notably the constant values of specific heat and the inability to fully match the 'true' fluid dynamic state vector at the nozzle exits. Similar to the equivalent species model, in order to match the important quantity of motor thrust, the pressure and velocity are set to exactly match those of the true exhaust mixture as given by the precursor CFD simulations. The temperature is recomputed using the gas constant of the air model and the equation of state. This typically raises the temperature at the nozzle exits for the perfect air simulations, making this model unsuitable for cases where the prediction of heat transfer is a primary concern. A brief summary of the different exhaust gas models is found in Table. 2

Table 2: CFD Run Matrix

Model	Species Present	Considers Reactions
Niu[9] Multi-species	CO_2, CO, Cl_2, Cl, H_2O, H_2, HCl, HO_2, H, N_2, NO, N, O_2, OH, O	Yes
Equivalent species	Equiv. ACM Gas, Equiv. AM Gas, Equiv. Air	No
Perfect Air	Equiv. Air	No

IV. Results

This section will detail the results of the CFD simulations for the unpowered cases, followed by the powered cases with the different exhaust gas models. Due to export restrictions, all quantitative results will be presented as a percent change from some other result, with neither original data set explicitly written. Meaningful analysis, however, is still provided as the effect of plumes and the various exhaust models will still be made clear by the percent changes.

A. Unpowered Abort Simulations

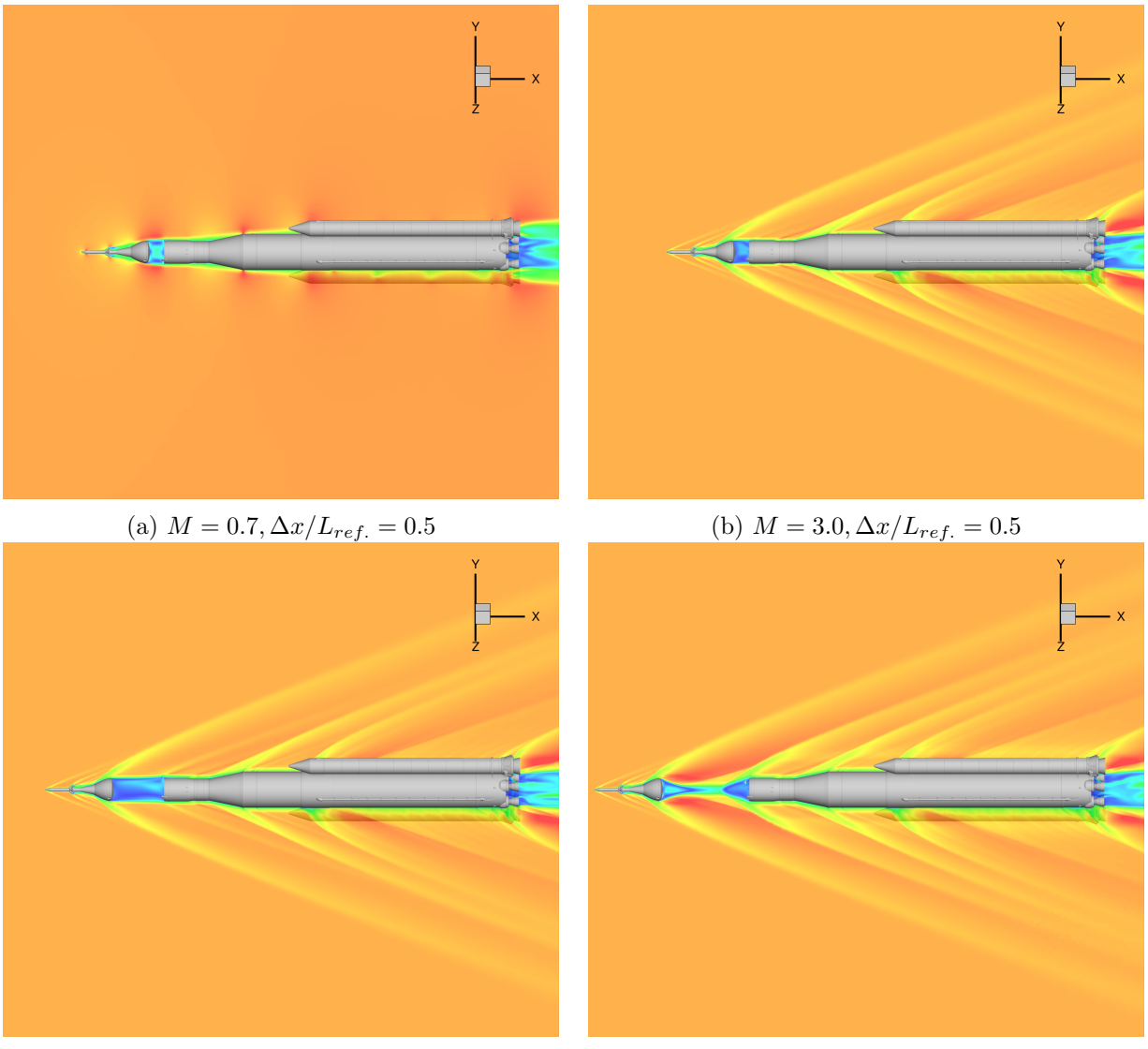

(a) $M = 0.7, \Delta x/L_{ref.} = 0.5$

(b) $M = 3.0, \Delta x/L_{ref.} = 0.5$

(c) $M = 3.0, \Delta x/L_{ref.} = 1.5$

(d) $M = 3.0, \Delta x/L_{ref.} = 2.5$

Figure 6: (a)-(d) Saturated pseudocolor contours of Mach number shown on a semi-transparent plane cutting the domain along the center-line of two AM nozzles for each of the unpowered cases.

In order to establish the effect that the AM and ACM plumes have on the flow field and on the drag of the aborted core stage, the results of the unpowered CFD simulations are presented first. Contours of Mach number are shown on a cut-plane through the domain for each of the unpowered cases in Figs. 6a-6d. The case depicted in Fig. 6a displays locally supersonic flow over shoulders that are expected with high sub-sonic Mach numbers. At the supersonic Mach numbers considered in Figs. 6b and 6c, attached shocks can be

seen to form at the tip of the LAV, over the AM nozzles, the ogive of the MPCV, the windward facing side of the launch vehicle stage adaptor (LVSA), booster forward attachments, and the booster aft skirts.

All thee cases discussed so far have displayed some recirculation region immediately downstream of the heat shield on the MPCV. The case depicted in Fig. 6d, however, displays a drastic difference in this region. At this LAV offset distance of $\Delta x/L_{ref.} = 2.5$, the LAV is far enough upstream to allow a short wake to form downstream of the heat shield as well as the beginnings of a strong bow shock ahead of the cavity at the leading edge of the core stage. As will be shown in the following sections, this geometric configuration will become one of interest in the study of the different gas models.

Table 3: Summary of Core Stage Axial Force Coefficient for Unpowered Simulations

$\Delta x/L_{ref.}$	Mach Number	CA (relative)
0.5	0.7	-
0.5	3.0	+39.43%
1.5	3.0	+43.10%
2.5	3.0	+78.99%

Baseline expectations for the powered simulations can be set by evaluating the effect of the different LAV offsets and freestream Mach number on the core stage drag from the unpowered cases. This is presented in Table 3 as percent changes in the axial force coefficient for all unpowered cases with respect to the $M = 0.7$, $\Delta x/L_{ref.} = 0.5$ case. Moving from $M = 0.7$ to $M = 3.0$ at $\Delta x/L_{ref.} = 0.5$ shows a fairly large increase in CA as the freestream Mach number becomes supersonic. The differences in the $M = 3.0$ solutions at $\Delta x/L_{ref.} = 0.5$ and $\Delta x/L_{ref.} = 1.5$, however, are fairly close, and this will become a recurring observation throughout the rest of this work. As seen in Figs. 6b and 6c, this is because at these conditions, the wake of the MPCV does not have space to break apart and instead simply extends to the leading edge of the core stage. This yields very similar flow topologies between the two cases. Finally, as stated before, the solution at $\Delta x/L_{ref.} = 2.5$ displays different behavior from the others as the LAV wake and core stage bow shock start to become present, significantly raising the drag on the aborted core stage as is seen in the final row of Table 3.

B. Powered Abort Simulations: Chemically-Reacting

The first set of powered abort simulations will use the chemically reacting, 15-species, 30-reaction exhaust gas model. The details of this model can be found in Sec. III B. Considering the test matrix shown in Table 1, each simulation will consider a relevant 'low'- and 'high'-thrust AM thrust condition while the ACM is held in the 'null' configuration. Contours of Mach number are shown on a cut-plane through the domain for some of the powered cases with the finite rate chemistry model in Figs. 7a-7d. For brevity, only the cases considering the low-thrust AM conditions are shown as the topological differences in the flow fields obtained with low- and high-thrust AM conditions are not as severe as the differences between the different LAV offset distances.

One notable difference is the dramatic expansion the AM plumes undergo in the cases considering the supersonic freestream Mach number (Figs. 7b-7d) compared to the subsonic case (Fig. 7a). This is due to a significantly lower ambient pressure corresponding to a higher altitude in the flight trajectory at this Mach number. In addition to this large expansion, the AM plumes in the supersonic cases are forced into a tight region near the body, causing the plumes to impinge on the ogive of the LAV and along the leading portions of the aborted core stage.

The effect of the LAV offset distance yields similar effects to those seen in the unpowered cases. That is, at $\Delta x/L_{ref.} = 0.5$ and $\Delta x/L_{ref.} = 1.5$, an uninterrupted wake extends from the trailing edge of the LAV to the leading edge of the aborted core stage. At $\Delta x/L_{ref.} = 2.5$, however, there is enough space aft of the LAV for both the AM plumes to be entrained into the wake and the beginnings of a bow shock to form on the leading edge of the core stage, significantly altering the flow topology. To investigate this further, Figs. 8a-8d show color contours of the mean gauge pressure on a cut-plane through the domain along with a handful of streamlines for the low- and high-thrust $M = 3.0$ cases at $\Delta x/L_{ref.} = 1.5$ and $\Delta x/L_{ref.} = 2.5$.

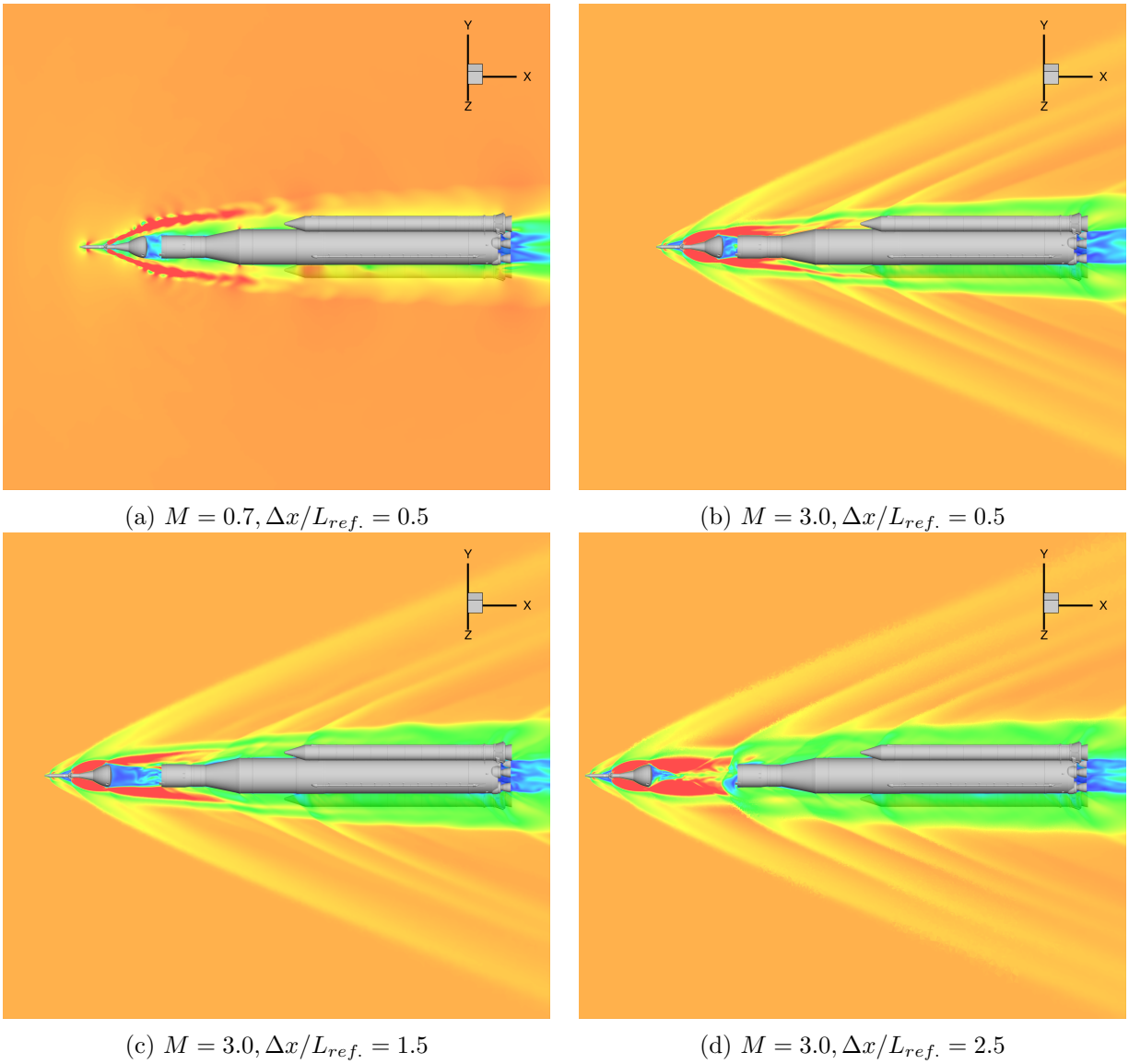

(a) $M = 0.7, \Delta x/L_{ref.} = 0.5$

(b) $M = 3.0, \Delta x/L_{ref.} = 0.5$

(c) $M = 3.0, \Delta x/L_{ref.} = 1.5$

(d) $M = 3.0, \Delta x/L_{ref.} = 2.5$

Figure 7: (a)-(d) Saturated pseudocolor contours of Mach number shown on a semi-transparent plane cutting the domain along the center-line of two AM nozzles for each of the powered cases using the chemically reacting exhaust gas model.

The flow is generally similar along the length of the LAV between all cases, though the extent of the plume region is larger in the high-thrust solutions. Differences begin to arise in the shape and size of the recirculation bubble aft of the LAV, however, as its large size in the $\Delta x/L_{ref.} = 1.5$ cases causes streamlines emanating from the freestream and AM nozzles to barely enter or entirely avoid the region. In the $\Delta x/L_{ref.} = 2.5$ cases, the bubble is significantly smaller and constrained to a region just under the heat shield. This shrinking of the recirculation region allows streamlines to accelerate around the edges of the bubble and form a supersonic wake and recompression shock as is evident by the sharp red contours that form at the intersection of the two sets of streamlines aft of the LAV in Figs. 8c and 8d. Note that the flow fields in Figs. 8c and 8d show that the 'upper' portion of the bow shock in the frame is pushed slightly further downstream than the 'lower' portion. This is the result of two of the four AM nozzles having slightly larger diameters in order to naturally induce an angle-of-attack into the LAV trajectory during abort, directing it away from the trajectory of the aborted core stage.

Table 4 summarizes the axial force coefficients obtained from the powered simulations using the chemically

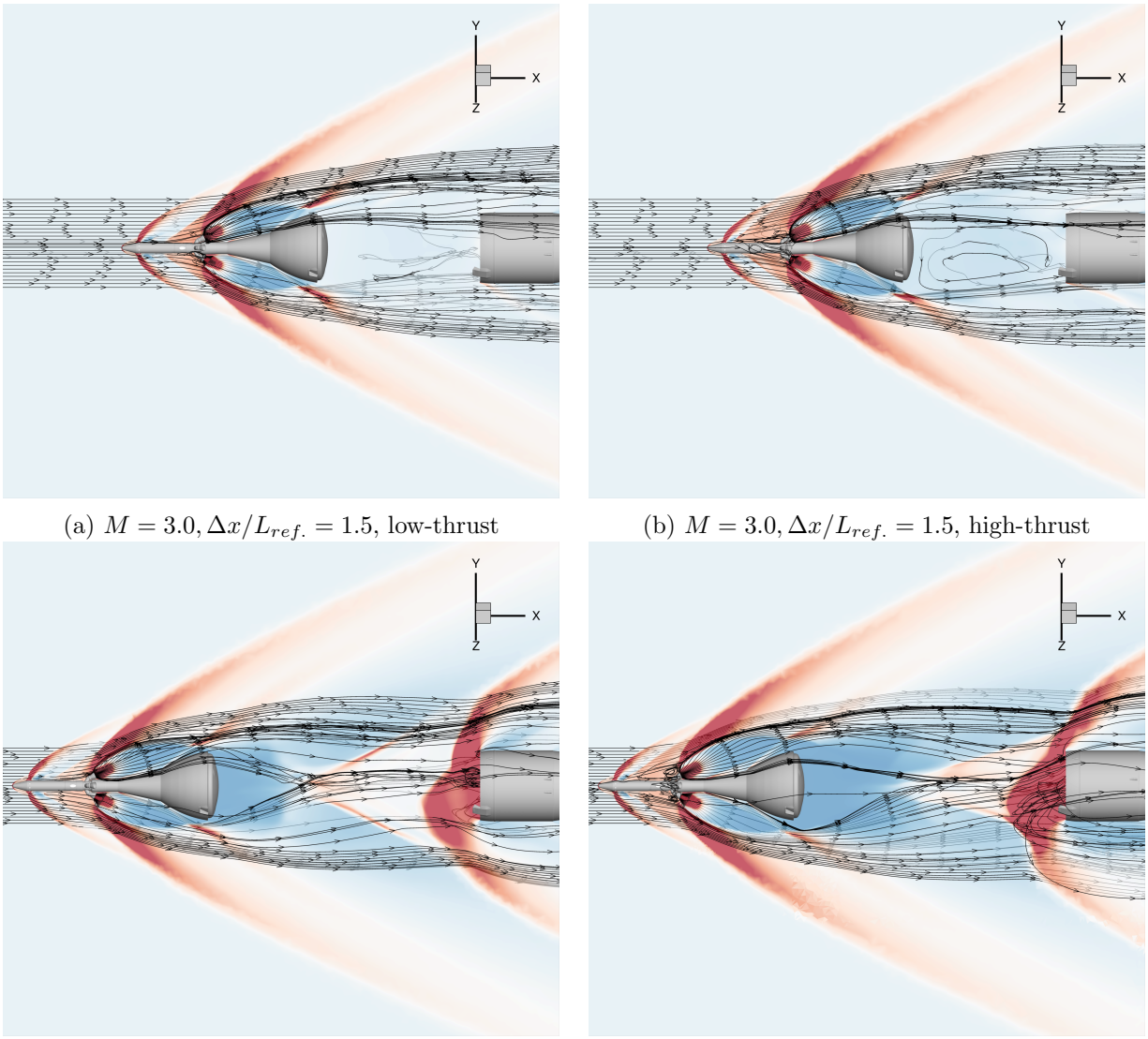

(a) $M = 3.0, \Delta x/L_{ref.} = 1.5$, low-thrust

(b) $M = 3.0, \Delta x/L_{ref.} = 1.5$, high-thrust

(c) $M = 3.0, \Delta x/L_{ref.} = 2.5$, low-thrust

(d) $M = 3.0, \Delta x/L_{ref.} = 2.5$, high-thrust

Figure 8: Saturated pseudocolor contours of mean gauge pressure shown on a semi-transparent plane cutting the domain along the center-line of two AM nozzles for the $M = 3.0, \Delta x/L_{ref.} = 1.5$, (a) low-thrust and (b) high-thrust cases and the $M = 3.0, \Delta x/L_{ref.} = 2.5$ (c) low-thrust and (d) high-thrust cases, all using the chemically reacting exhaust gas model.

reacting model. The results are shown as percent changes with respect to the associated unpowered case. That is, positive values indicate a larger CA predicted by the powered cases compared to the unpowered cases, and negative values indicate the opposite. Note the additional independent variable 'AM Thrust' for the powered simulations. Starting with the first two rows of Table 4, corresponding to the subsonic freestream cases, it can be observed that the presence of the ACM and AM plumes raises the axial force coefficient on the aborted core stage. Furthermore, increasing AM thrust slightly reduces CA compared to a lower thrust solution – but not significantly. At the supersonic Mach numbers, however, the presence of the plumes slightly decreases CA, likely due to strong bow shocks forming upstream of the ACM and AM nozzles lowering the momentum of the downstream flow. This trend is consistent for both $\Delta x/L_{ref.} = 0.5$ and $\Delta x/L_{ref.} = 1.5$, but again, at $\Delta x/L_{ref.} = 2.5$, much different results are observed. Not only does CA now increase with the presence of the plumes, the result becomes very sensitive to the AM thrust level – doubling the relative CA at the higher thrust level compared to the lower thrust level.

Table 4: Summary of Core Stage Axial Force Coefficient for Powered Simulations Using a Finite Rate Chemistry Model

$\Delta x/L_{ref.}$	Mach Number	AM Thrust	CA (relative)
0.5	0.7	Low	+7.37%
0.5	0.7	High	+4.30%
0.5	3.0	Low	-12.62%
0.5	3.0	High	-16.52%
1.5	3.0	Low	-5.03%
1.5	3.0	High	-7.25%
2.5	3.0	Low	+32.59%
2.5	3.0	High	+79.15%

The relationship between core stage drag and the LAV offset, freestream Mach number, and AM thrust level is then highly-nonlinear, and no clear functional relationship is easily determined. For example, from the results of the unpowered simulations, a correlation between increasing LAV offset distance and increasing CA could be inferred, but no similar statement can be made for the powered simulations. The results do not show monotonic behavior of CA with respect to any of the independent variables. The following subsections will attempt to provide an understanding of these complex physics using surface pressure and sectional loads analyses.

1. Surface Pressure Analysis: Chemically Reacting

Figs. 9a and 9b show the differences in the surface pressure coefficients from the $M = 0.7, \Delta x/L_{ref.} = 0.5$ low-thrust and unpowered case and the high-thrust and unpowered case, respectively. The color scale is such that red implies a positive difference, and thus larger surface pressures for the powered cases, white shows differences close to zero, and blue shows negative differences. Starting near the tip of the LAV for both figures, it can bee seen that the presence of the ACM plumes causes a lower pressure as the attached shock that forms there in the unpowered cases is 'bowed' out and forced off the body. The high pressure region that follows is immediately downstream of the ACM nozzles. Similar pressures continue along the tower until another high pressure region just downstream of the AM nozzles is observed. Fig. 9b shows a larger high pressure region due to the increased AM thrust. Following this, the surface pressure is generally higher along the ogive of the MPCV and onto the leading edges of the core stage and the windward-angled face of the LVSA. This is consistent with the slightly increased CA that are observed for the powered cases in Table 4. Downstream of the LVSA, the differences in the surface pressure are minor.

Similar figures of the difference in surface pressures between the powered and unpowered $M = 3.0$, $\Delta x/L_{ref.} = 0.5$ cases are shown in Figs. 10a and 10b. Given the high freestream Mach number and low ambient pressure at this point in the flight trajectory, the AM plumes undergo significant expansion and are turned onto the ogive of the MPCV, creating a large positive difference in surface pressure in Fig. 10. Majority of the core stage, however, shows little to no differences in the surface pressure between the powered and unpowered cases. Since Table 4 showed that the presence of the plumes lowers CA on the core stage, which was attributed to the strong shocks that form upstream of the ACM and AM nozzles weakening the downstream shocks, the primary drag producing surface must then be the cavity at the leading edge of the core stage, and not any other surface on the core stage. This will be shown in more detail in the following subsection on sectional loads analysis, but this can also be qualitatively studied by inspection of Fig. 11, where the lower surface pressure predicted by the powered case relative to the unpowered one is shown in the cavity at the leading edge of the core stage for the high-thrust $M = 3.0$, $\Delta x/L_{ref.} = 0.5$ simulation. The red contours corresponding to the AM plumes impinging on the windward facing surface of the LVSA can also be seen. Similar conclusions about the differences in the surface pressure in the cavity are obtained for the $\Delta x/L_{ref.} = 1.5$ and $\Delta x/L_{ref.} = 2.5$ cases, and thus, they are omitted here. Though in those cases, as will be shown, the pressure in the cavity grows significantly with increasing LAV offset.

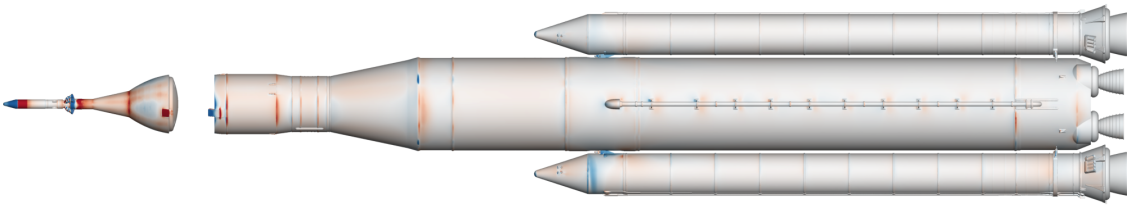

(a) $C_{p,low-thrust} - C_{p,unpowered}$

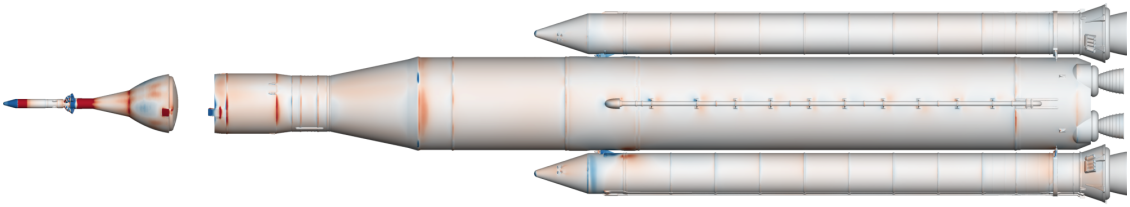

(b) $C_{p,high-thrust} - C_{p,unpowered}$

Figure 9: Saturated color contours of the difference in C_p between the (a) low-thrust powered and unpowered and (b) high-thrust powered and unpowered $M = 0.7, \Delta x/L_{ref.} = 0.5$ cases shown on the surface of the geometry.

2. *Sectional Loads Analysis: Chemically Reacting*

The surface pressure analysis in the previous section clearly shows the effect of the plumes on the LAV, but the differences in surface pressure on the core stage between the powered and unpowered cases were seemingly small over the majority of the vehicle. When the view was adjusted to look into the cavity at the leading edge of the core stage, however, it could qualitatively be determined that this was the primary drag producing surface on the core stage. To quantify this, and to further analyze the effect of the chemically-reacting exhaust gas on the core stage drag, a sectional loads/line loads analysis is performed here. An introduction to sectional load analysis is beyond the scope of this paper, but many instances of its application to slender launch vehicles can be found in the literature.[11–13]

Figs. 12a-12d display the results of a sectional loads analysis performed for each of the cases studied thus far. Typically, the results of sectional loads analysis are presented as a rate of change of the coefficient of interest with respect to a non-dimensional streamwise position. Here, however, in order to overcome the very large rates that are seen in the cavity for the $\Delta x/L_{ref.} = 2.5$ cases, the coefficient is plotted as a cumulative value that grows as the streamwise position is marched downstream from the leading edge - reaching its full value at the trailing edge of the vehicle. Most cases display at least some differences in the cumulative value of CA near the leading edge, but the differences become most notable for the $\Delta x/L_{ref.} = 2.5$ cases, for all of the reasons already mentioned, but now it can be seen that over 60% of the drag in the powered cases is generated from the cavity alone. This is compared to only about 28% in the unpowered case. This shows a very large sensitivity to the presence and strength of the AM plumes at this LAV offset, and it will be a case of interest when studying the simplified exhaust gas models. To some extent, a similar observation can be made for the $\Delta x/L_{ref.} = 1.5$ cases, but as shown in the previous sections and in Fig. 8, the majority of the plume simply passes by the cavity with only a portion finding its way into the recirculation region aft of the LAV.

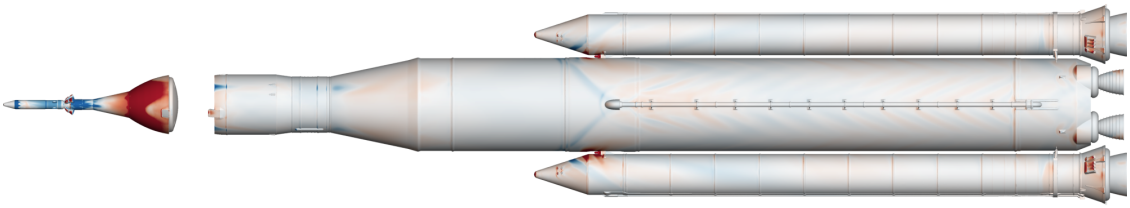

(a) $C_{p,low-thrust} - C_{p,unpowered}$

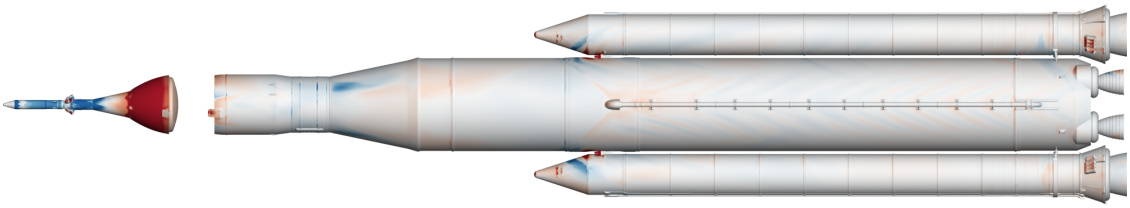

(b) $C_{p,high-thrust} - C_{p,unpowered}$

Figure 10: Saturated color contours of the difference in C_p between the (a) low-thrust powered and unpowered and (b) high-thrust powered and unpowered $M = 3.0, \Delta x/L_{ref.} = 0.5$ cases shown on the surface of the geometry.

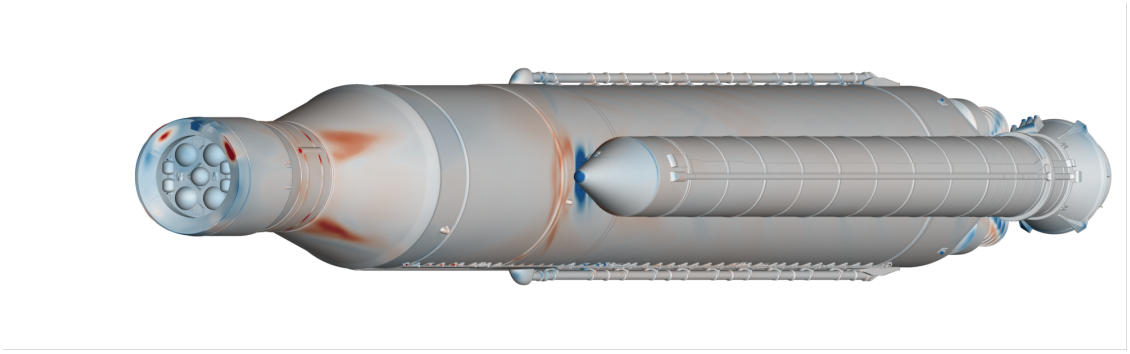

$C_{p,high-thrust} - C_{p,unpowered}$

Figure 11: Perspective view of saturated color contours of the difference in C_p between the high-thrust powered and unpowered $M = 3.0, \Delta x/L_{ref.} = 0.5$ case shown on the surface of the geometry.

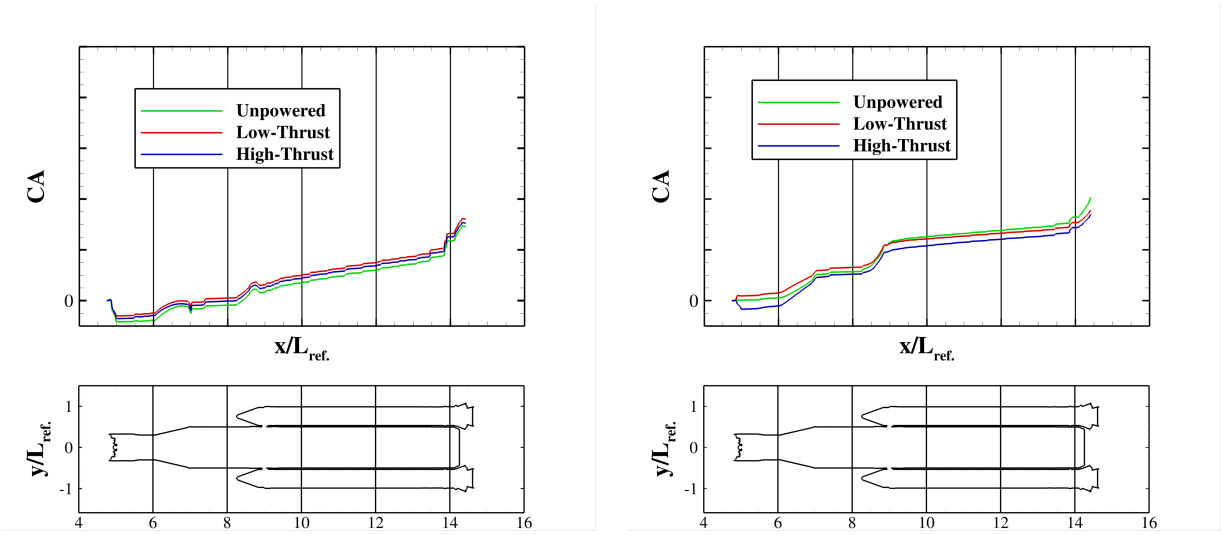

(a) $M = 0.7$, $\Delta x/L_{ref.} = 0.5$

(b) $M = 3.0$, $\Delta x/L_{ref.} = 0.5$

(c) $M = 3.0$, $\Delta x/L_{ref.} = 1.5$

(d) $M = 3.0$, $\Delta x/L_{ref.} = 2.5$

Figure 12: (a)-(d) Cumulative CA along the body of the aborted core stage and boosters from a sectional loads analysis for each of the unpowered and powered chemically-reacting cases.

C. Powered Abort Simulations: Single Equivalent Species

The next set of simulations considers a single equivalent species for the ACM and the AM exhausts gases as described in Sec. III B. A third species is defined in the freestream that is equivalent to calorically-imperfect air. There are no chemical reactions between any of the species, and the only varying independent parameters are the specific heats as defined in Sec. III B. Because of the subtle differences between the low- and high-thrust cases, only the low-thrust AM cases are considered here onward, with the exception of the highly-sensitive $M = 3.0$, $\Delta x/L_{ref.} = 2.5$ cases.

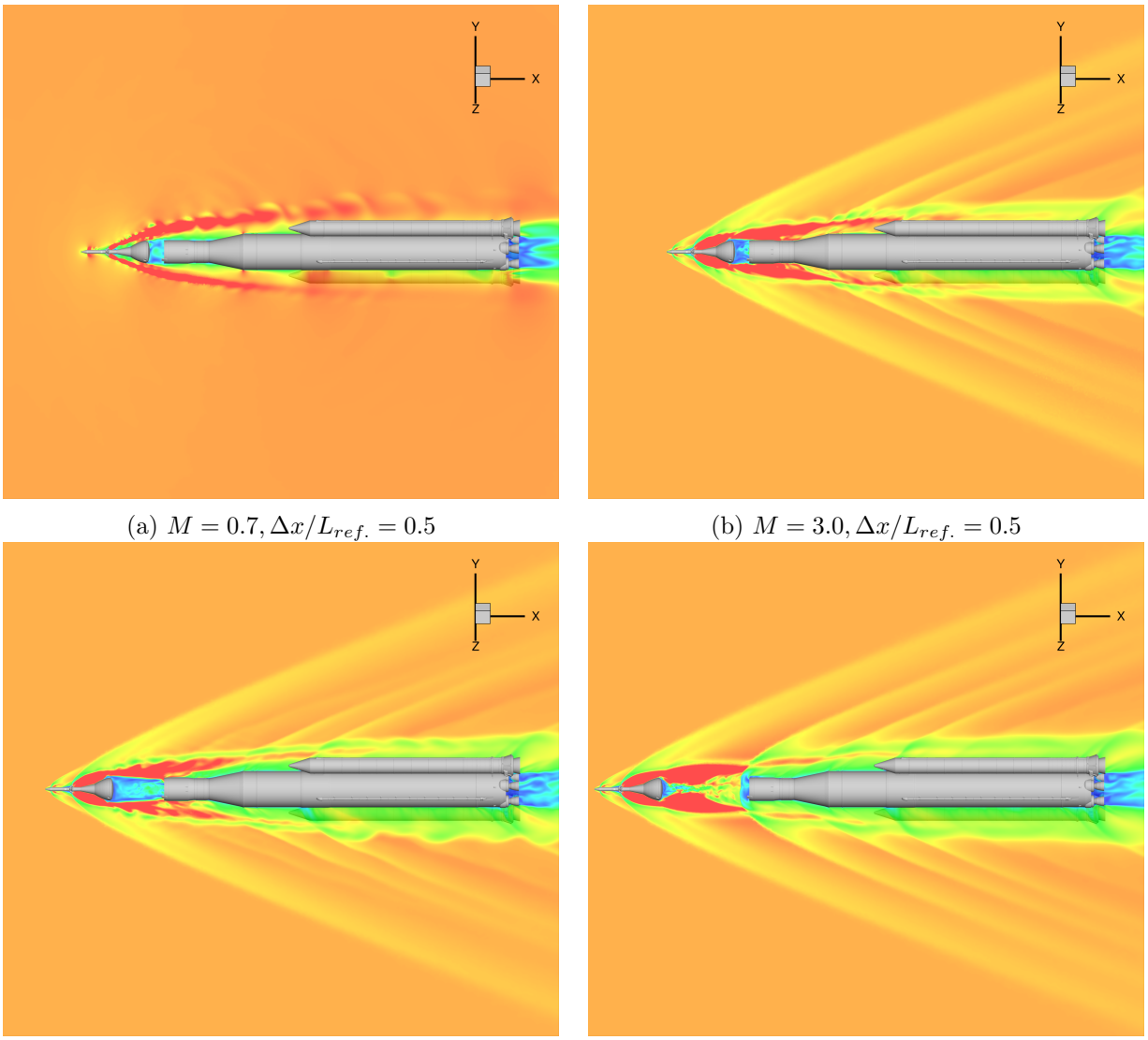

(a) $M = 0.7, \Delta x/L_{ref.} = 0.5$

(b) $M = 3.0, \Delta x/L_{ref.} = 0.5$

(c) $M = 3.0, \Delta x/L_{ref.} = 1.5$

(d) $M = 3.0, \Delta x/L_{ref.} = 2.5$

Figure 13: (a)-(d) Saturated pseudocolor contours of Mach number shown on a semi-transparent plane cutting the domain along the center-line of two AM nozzles for each of the low-thrust powered cases using the single equivalent species exhaust gas model.

Figs. 13a-13d show color contours of Mach number on a slice through the domain for each of the low-thrust cases using the single equivalent species model. In comparison to Figs. 7, some notable differences are readily observed. Specifically, the AM plumes in the $M = 0.7$ freestream case in Fig. 13a maintains high speed flow further downstream relative to its chemically reacting counterpart in Fig. 7a. To some extent, this is true for all of the cases as the composition of the chemically reacting exhaust gas likely undergoes changes as it expands and cools during its downstream advection. What is key, however, is the effect that

the changes in the mixture composition may have on the drag of the aborted core stage.

Table 5: Summary of Core Stage Axial Force Coefficient for Powered Simulations using a Single Equivalent Species Model

$\Delta x/L_{ref.}$	Mach Number	AM Thrust	CA (relative)
0.5	0.7	Low	+6.04%
0.5	3.0	Low	+5.38%
1.5	3.0	Low	+7.76%
2.5	3.0	Low	-0.84%
2.5	3.0	High	+16.49%

Table 5 summarizes the core stage drag for the single equivalent species cases shown as a percent change relative to the associated case with finite rate chemistry. While ideally, all the results obtained using the single equivalent species exhaust gas model would be conservative (lower CA relative to the chemically reacting cases), the increases that are observed are all within +10% with the exception of the highly sensitive $M = 3.0$, $\Delta x/L_{ref.} = 2.5$ case with high-thrust, which is encouraging. To try to understand this and where the differences in drag are occurring, the surface pressure and sectional loads analyses will be performed again for the equivalent species cases in the following sub-sections.

1. Surface Pressure Analysis: Single Equivalent Species

Figs. 14a and 14b show the differences in the pressure coefficient obtained with the equivalent single species and the chemically reacting exhaust gas models on the surface of the body at low-thrust $M = 3.0$, $\Delta x/L_{ref.} = 0.5$ and high-thrust $\Delta x/L_{ref.} = 2.5$, respectively. These cases represent 'good' ($\Delta x/L_{ref.} = 0.5$) and 'fair' ($\Delta x/L_{ref.} = 2.5$) agreement with respect to the CA predicted by the chemically reacting exhaust gas model. The figures show relatively small differences over majority of the LAV and core stage, with the primary differences being in the cavity at the leading edge of the core stage. The red colored contours represent regions of positive differences, and hence, a larger C_p for the case with the equivalent species model. From this perspective, it is clear that the equivalent species cases have larger pressures in the cavity, leading to the positive percent changes of CA compared to the chemically reacting cases that are shown in Table 5.

A forthcoming line loads analysis on the core stage will make this more clear, but it can be concluded now that the cavity is again the primary drag producing surface on the aborted core stage, and any differences between models that occur are driven by this region.

2. Sectional Loads Analysis: Single Equivalent Species

The sectional/lines loads analysis is repeated in this section in order to further investigate the effect of modeling the ACM and AM exhaust gas with a single equivalent species. Figs. 15a-15d show the cumulative value of CA on the aborted core stage versus streamwise position for the unpowered, chemically reacting, and equivalent species exhaust gas models. Overall, good agreement between the two exhaust gas models is seen, with the primary differences occurring near the cavity at the leading edge of the core stage. Expectedly, this is most evident for the case shown in Fig. 15d. For these cases, approximately 70% of the cumulative CA is generated for both models in the cavity alone.

3. Evaluation of the Single Equivalent Species Model

The cavity has been shown multiple times to be arguably the most important surface on the core stage in terms of aerodynamic drag. Small differences in pressure here yield much different values for CA on the entire core stage when using the different exhaust gas models. These differences may arise for a number of reasons including different plume widths, temperatures, and additional reactions that occur in the chemically reacting simulations that are not captured when using the equivalent species model. This is because the single equivalent species model is essentially 'frozen' at the properties of the true exhaust gas mixture at the point in space and time that was used to create it. That is, the equivalent species gas constant and

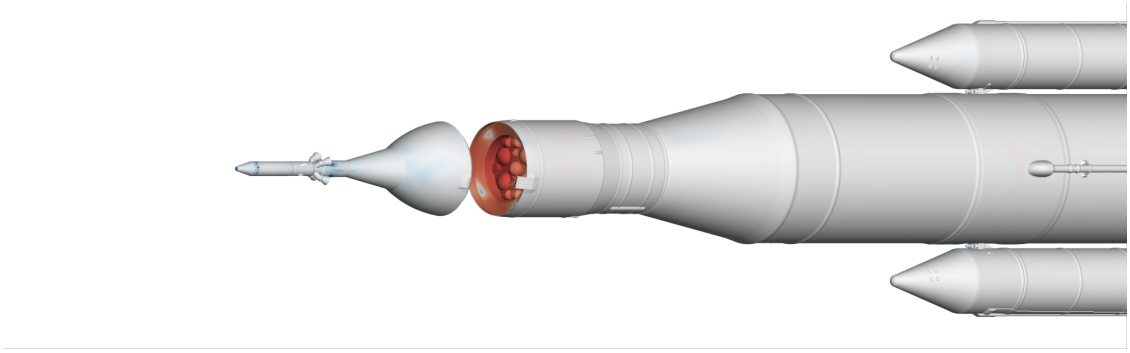

(a) $C_{p,equiv.} - C_{p,chem.react.}$, $M = 3.0, \Delta x/L_{ref.} = 0.5$

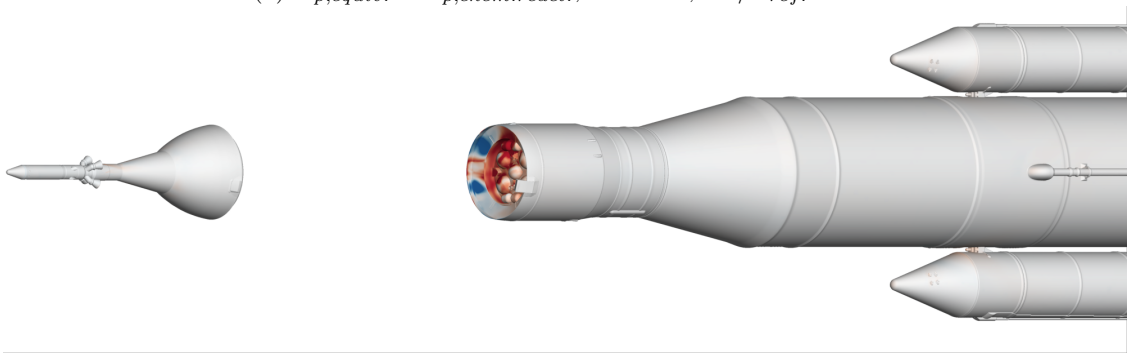

(b) $C_{p,equiv.} - C_{p,chem.react.}$, $M = 3.0, \Delta x/L_{ref.} = 2.5$

Figure 14: Perspective view of saturated surface color contours of the difference in C_p between the (a) low-thrust $M = 3.0, \Delta x/L_{ref.} = 0.5$ and (b) high-thrust $M = 3.0, \Delta x/L_{ref.} = 2.5$ powered cases using an equivalent species and chemically reacting exhaust gas model, respectively.

molecular weight do not change when the gas heats or cools significantly, even if the true mixture would. Thus, a good representation of the equivalent species deviation from the true mixture would be a qualitative analysis of the mass fraction of a reactant in the fuel mixture – in this case, H_2.

Figs. 16a and 16b show the local mass fraction of H_2 for the $M = 3.0$, low-thrust case at $\Delta x/L_{ref.} = 0.5$ and the $M = 3.0$, high-thrust case at $\Delta x/L_{ref.} = 2.5$, respectively. For the case with the closer LAV offset, the mass fraction of H_2 stays relatively constant from the AM nozzle exits to the edge of the frame, with the exception of the plume shear layer past the leading edge of the aborted core stage. For the larger LAV offset, however, the local mass fraction of H_2 changes significantly as the available H_2 is heated as it passes the core stage bow shock. The concentration that ultimately reaches the core stage cavity is different than the concentration that left the AM nozzles, and thus, the gas mixture that ultimately reaches the core stage cavity is different between the chemically reacting and equivalent species cases (*e.g.,* different molecular weight, transport properties, and specific heats). Despite these differences, Table 5 summarized that the relevant quantity of CA on the core stage could be predicted within 10% for all cases with the exception of the high-thrust case at $\Delta x/L_{ref.} = 2.5$ which saw differences above 15%. This affirms that aerodynamic drag can be predicted using a single equivalent species to model the exhaust gas, provided that the composition of the mixture does not change significantly. For the high-thrust case at $\Delta x/L_{ref.} = 2.5$, the differences in the predicted composition of the gas near the leading edge cavity may have been too large between the chemically reacting and equivalent species case to provide better agreement.

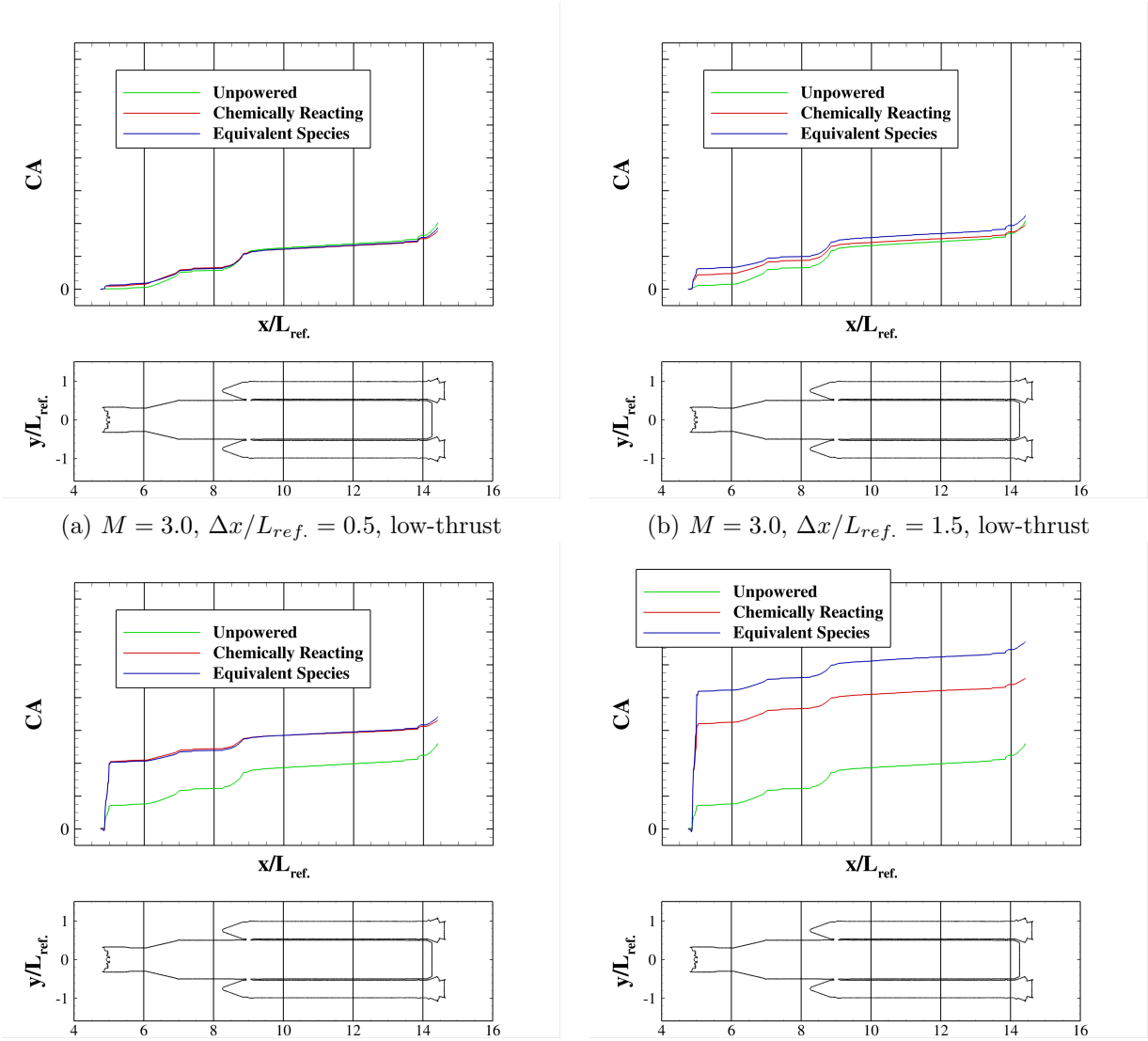

(a) $M = 3.0$, $\Delta x/L_{ref.} = 0.5$, low-thrust

(b) $M = 3.0$, $\Delta x/L_{ref.} = 1.5$, low-thrust

(c) $M = 3.0$, $\Delta x/L_{ref.} = 2.5$, low-thrust

(d) $M = 3.0$, $\Delta x/L_{ref.} = 2.5$, high-thrust

Figure 15: (a)-(d) Cumulative CA along the body of the aborted core stage and boosters from a sectional loads analysis for a selection of the unpowered and powered cases with the chemically reacting and equivalent species exhaust gas models.

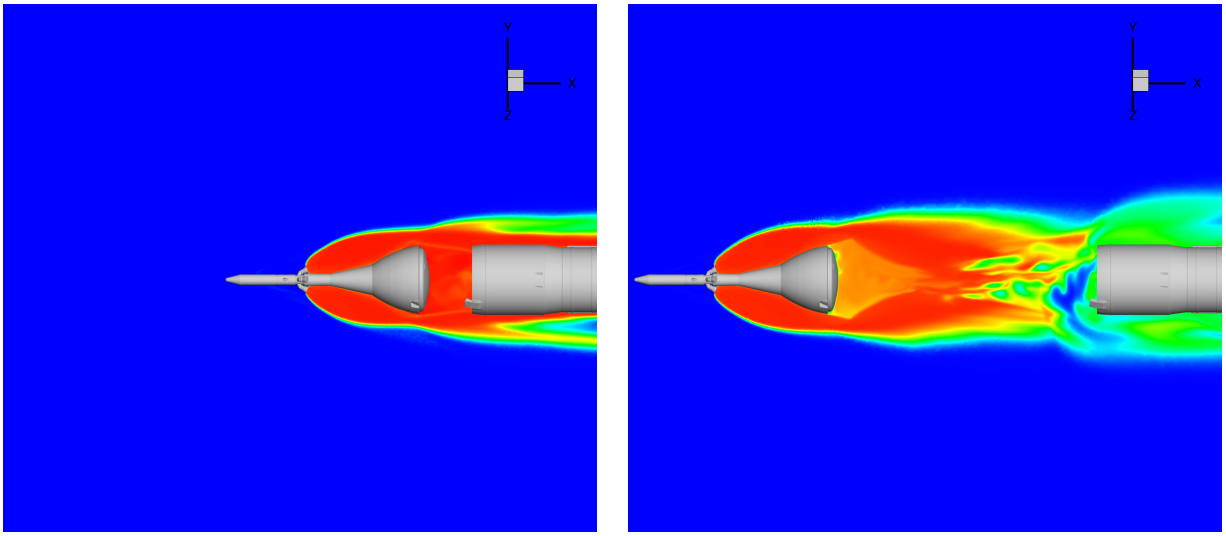

(a) $M = 3.0, \Delta x/L_{ref.} = 0.5$, low-thrust (b) $M = 3.0, \Delta x/L_{ref.} = 2.5$, high-thrust

Figure 16: (a)-(b) Saturated pseudocolor contours of the mass fraction of H_2 obtained by the chemically reacting simulations shown on a semi-transparent plane cutting the domain along the center-line of two AM nozzles.

D. Powered Abort Simulations: Calorically Perfect Air

Finally, the case of modeling the exhaust gases as calorically perfect air is considered. Any short-comings of the single equivalent species (*e.g.*, constant molecular weight and gas constant) are also inherited here, with the addition of being calorically perfect (constant specific heats). Despite this, whether or not the quantities of interest can be obtained using such a simple but prolific model is studied here.

Figs. 17a-17d show color contours of Mach number on a cut plane through the center of the domain for the powered cases using the perfect air model. Upon direct comparison with Figs. 7a-7d, which show the same contours for the powered cases with the chemically reacting model, a few observations can be made. First, once the plumes pass the leading edge of the core stage in the chemically reacting cases, they stay very close to the body and maintain high speeds. In the perfect air cases, however, there is a relatively slow region of flow compared to the plume gas speed that starts at the leading edge of the core stage in some cases and extends over the windward facing surface of the LVSA and beyond. This slow region diverts the plume gases and pushes them off of the body. The effect that this may have on the surface pressure on the core stage will be studied in the following subsection.

For the perfect air case depicted in Fig. 17d, the LAV wake is significantly wider than that of the chemically reacting case depicted in Fig. 7d. This may be due to a variety of reasons relating to differences in the gas modeling, but more importantly, the dominant drag producing surface of the core stage, that is, the cavity at the leading edge, is now exposed to a wide and (relatively) slow moving wake that blocks the high speed plume gas from impinging on it. Thus, lower values of CA relative to the chemically reacting cases can be expected here.

Table 6 shows CA on the core stage obtained with the perfect air exhaust gas model as a percent change relative to the associated case using the chemically reacting model. Overall, the agreement is good and is comparable to the results obtained with the single equivalent species model. As was predicted, however, the disagreement is greatest at the LAV offset of $\Delta x/L_{ref.} = 2.5$. Contrary to the single equivalent species results, which saw large over predictions of CA at these offsets, the results obtained with the perfect air model underpredict CA compared to the chemically reacting cases by approximately 20% for the aforementioned reasons.

Table 6: Summary of Core Stage Axial Force Coefficient for Powered Simulations using a Perfect Air Model

$\Delta x/L_{ref.}$	Mach Number	AM Thrust	CA (relative)
0.5	0.7	Low	+8.91%
0.5	3.0	Low	+5.81%
1.5	3.0	Low	+3.60%
2.5	3.0	Low	-18.25%
2.5	3.0	High	-20.68%

1. *Surface Pressure Analysis: Calorically Perfect Air*

Figs. 18a and 18b show the difference in C_p on the surface of the geometry between the perfect air and chemically reacting simulations. Blue contours represent lower values of C_p in the perfect air cases, white represents little to no differences, and red represents higher values for perfect air. For all cases shown, the difference contours shown on the surface are predominately white, meaning that there are little to no differences between each of the models in terms of surface pressure downstream of the leading edge cavity. This is encouraging and motivates the use of the single equivalent species and perfect air exhaust gas models when judiciously utilized for problems within their realm of applicability. Regardless, at $\Delta x/L_{ref} = 2.5$, depicted in Fig. 18b, the lower pressures in the cavity at the leading edge of the core stage are immediately obvious.

2. *Sectional Loads Analysis: Calorically Perfect Air*

The final analysis performed is that of sectional loads, comparing the loads predicted by the perfect air model to the results obtained thus far. The aforementioned conclusions are clearly seen in Figs. 19c and 19d

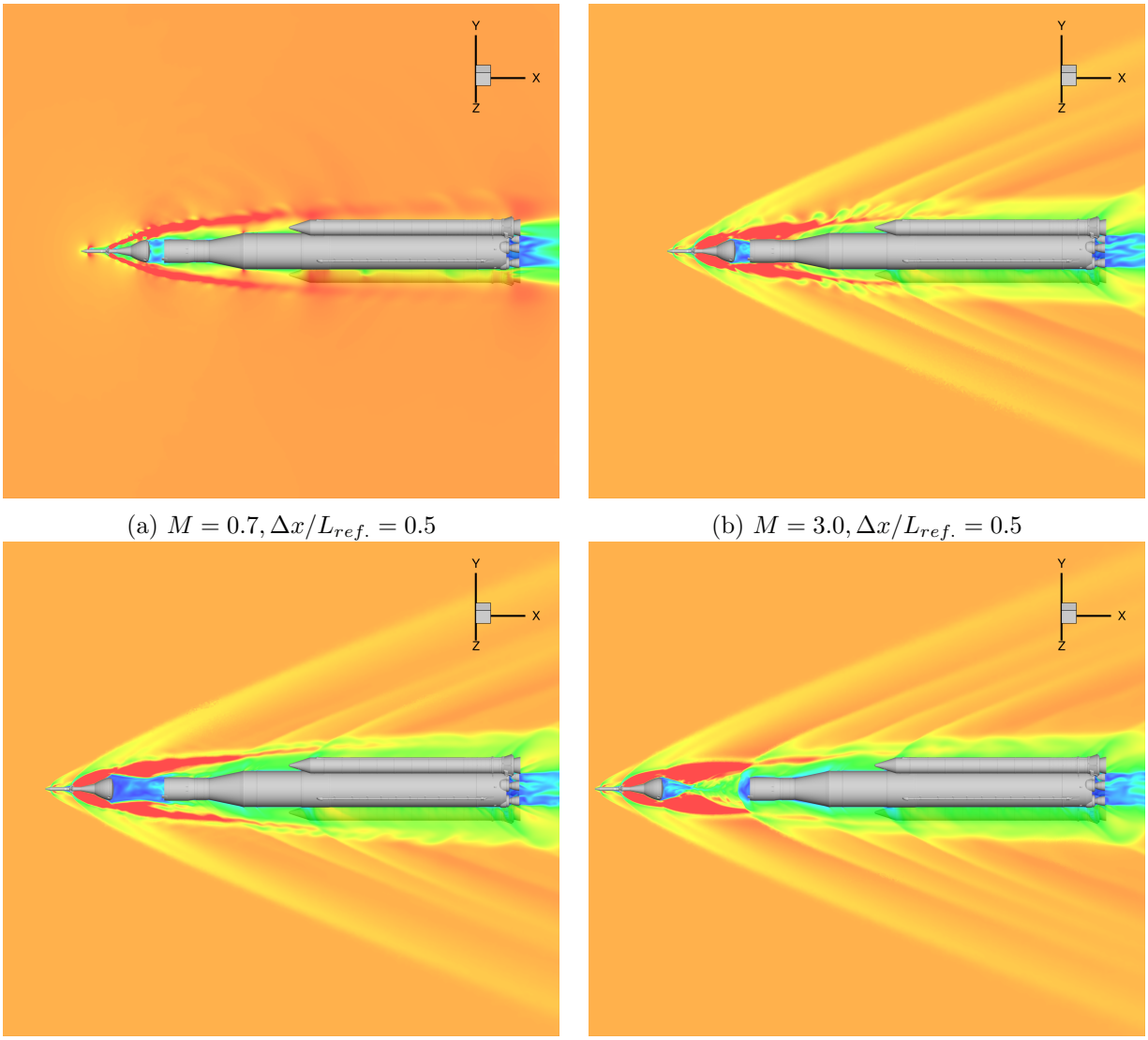

(a) $M = 0.7, \Delta x/L_{ref.} = 0.5$

(b) $M = 3.0, \Delta x/L_{ref.} = 0.5$

(c) $M = 3.0, \Delta x/L_{ref.} = 1.5$

(d) $M = 3.0, \Delta x/L_{ref.} = 2.5$

Figure 17: (a)-(d) Saturated pseudocolor contours of Mach number shown on a semi-transparent plane cutting the domain along the center-line of two AM nozzles for each of the low-thrust powered cases using the perfect air exhaust gas model.

where the cumulative values of CA near the cavity at the leading edge of the core stage do not rise as high for the cases considering perfect air. Because of this initial offset, this value of integrated CA is less than the value of CA predicted by the chemically reacting case - despite good agreement over the rest of the body.

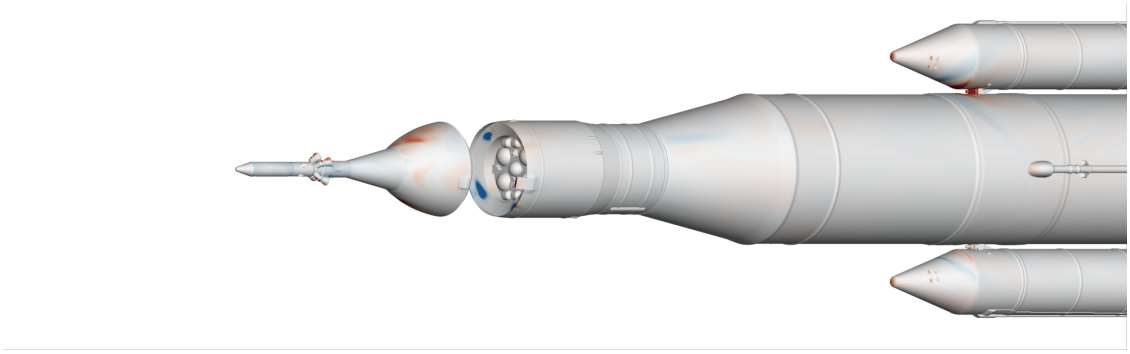

(a) $C_{p,equiv.} - C_{p,chem.react.}$, $M = 3.0, \Delta x/L_{ref.} = 0.5$

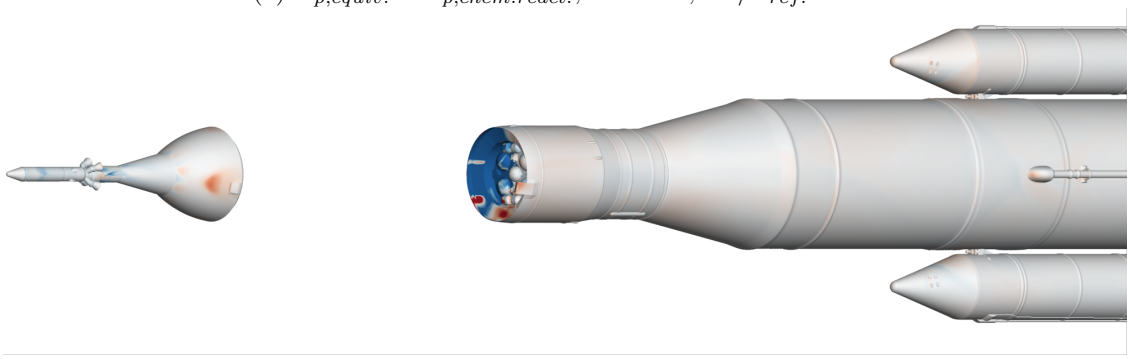

(b) $C_{p,equiv.} - C_{p,chem.react.}$, $M = 3.0, \Delta x/L_{ref.} = 2.5$

Figure 18: Perspective view of saturated surface color contours of the difference in C_p between the (a) low-thrust $M = 3.0, \Delta x/L_{ref.} = 0.5$ and (b) high-thrust $M = 3.0, \Delta x/L_{ref.} = 2.5$ powered cases using a perfect air and a chemically reacting exhaust gas model, respectively.

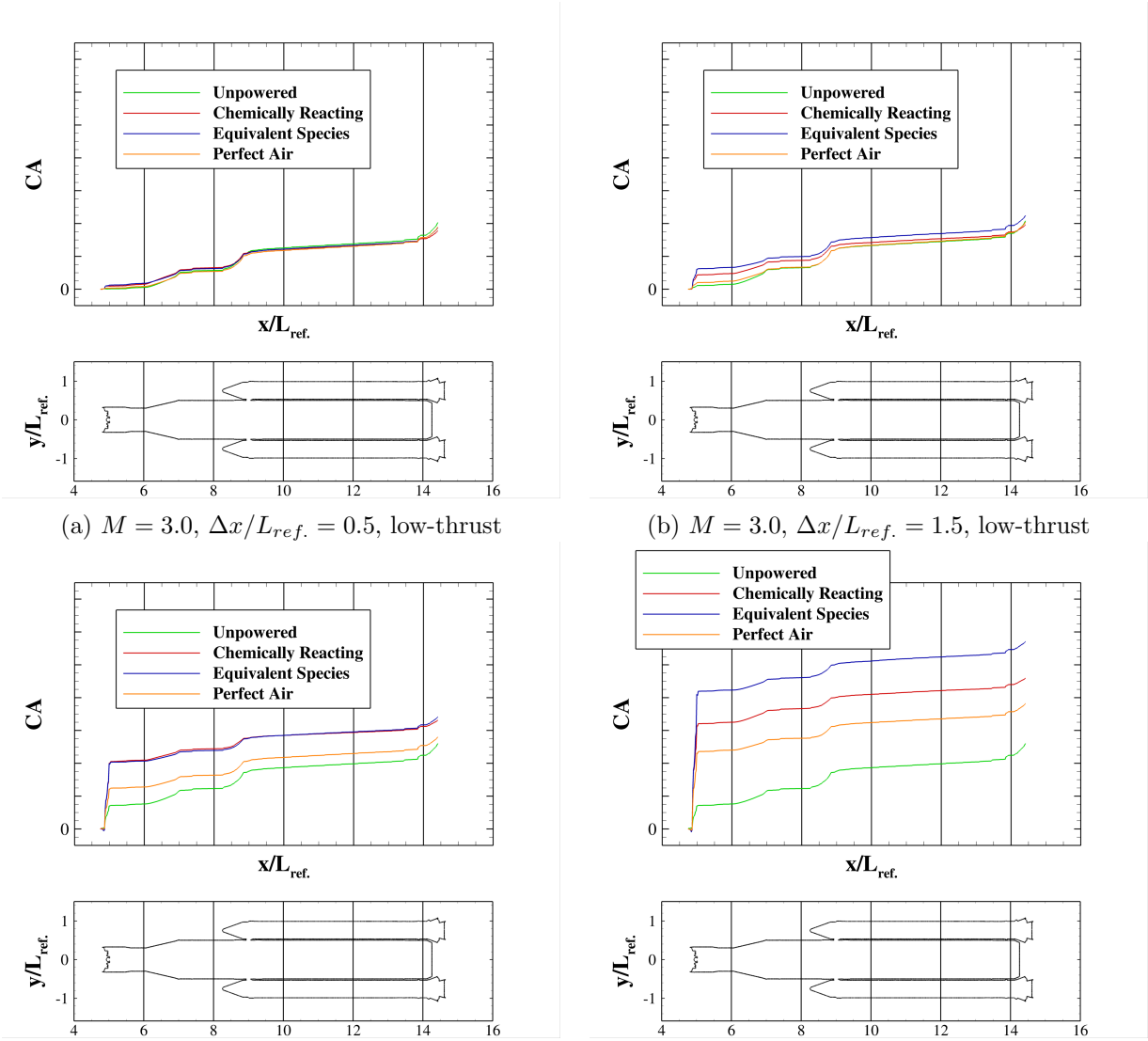

(a) $M = 3.0$, $\Delta x/L_{ref.} = 0.5$, low-thrust

(b) $M = 3.0$, $\Delta x/L_{ref.} = 1.5$, low-thrust

(c) $M = 3.0$, $\Delta x/L_{ref.} = 2.5$, low-thrust

(d) $M = 3.0$, $\Delta x/L_{ref.} = 2.5$, high-thrust

Figure 19: (a)-(d) Cumulative CA along the body of the aborted core stage and boosters from a sectional loads analysis for a selection of the unpowered and powered cases with the chemically reacting, equivalent species, and perfect air exhaust gas models.

V. Cost Comparison of Exhaust Gas Models

Beyond the differences in model accuracy, each of the methods considered thus far come with another set of factors for the engineer to consider. Ideally, an engineer would be provided an accurate model for the dominant chemical reactions present in a given problem, no more and no less, and then create entire CFD databases using finite rate chemistry. This, however, is rarely the case. The use of perfect air as an exhaust gas is not hard to find in the literature, and for good reason. The computational cost of solving a larger system of equations, one additional continuity equation for each specie present, modeling all reactions that occur during a single timestep, and dealing with increased stiffness of the linear system all make chemically reacting simulations untenable for large database work and often unnecessary for answers within engineering judgement. In this section, a converged solution from the above sections is restarted and allowed to run again using each of the exhaust gas models considered. The wall-clock time, measured in seconds, that it takes each simulation to conduct 20 Newton iterations will be recorded, and this process will be repeated at different core counts.

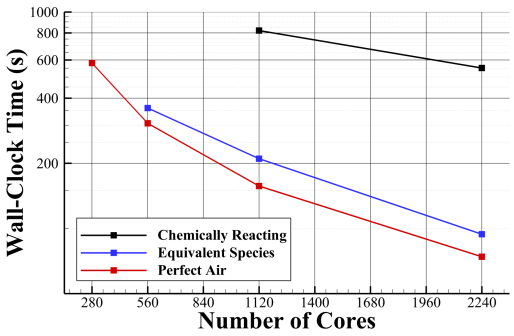

Figure 20: Plot of the wall-clock time in seconds required to advance a steady-state solution 20 Newtons iterations using each exhaust gas model.

The results of this analysis are shown in Fig. 20. Each simulation was conducted on Broadwell nodes, each with 28 cores. Given that there are approximately 270M cells, some cases could not start without running out of memory on the nodes, and thus, no data is shown for those cases in Fig. 20. Along these lines, the chemically reacting simulation could not be simulated until a minimum of 1200 cores were used, and even such, this simulation required more wall-clock time than the 280 core simulation that used perfect air. It is clear that if the perfect air cases are yielding unsatisfactory results, then the computational cost savings is irrelevant, but it is an important factor to consider for engineers tasked with database work. What may be encouraging is that the equivalent species model is only marginally slower than the perfect air model with the differences in cost arising from the three non-reacting species in the chemically reacting case (ACM, AM, and freestream gases) and the evaluation of the nonlinear functions for the specific heats.

The chemically reacting simulations are 4 times the cost of the equivalent species simulations solely in terms of wall-clock time. This does not account for how far the residuals in the system dropped over those 20 iterations, *e.g.*, one method, likely the chemically reacting method, may need more iterations to achieve the same drop in the residuals that the other methods achieve. This is beyond the scope of the current study and is not evaluated here. Its clear, however, that where an equivalent species model can be used, it should be, and any database generation may need the bulk of the simulations conducted with this simplified model while chemically reacting 'check' cases are run to ground the results.

VI. Conclusions

The Loci/CHEM compressible Navier-Stokes solver was used to conduct a series of viscous CFD simulations depicting Space Launch System post mode 1 abort scenarios using unstructured grids. The primary purpose of these simulations was to assess the accuracy of ACM and AM plume modeling using simplified models for the exhaust gases. The metric for comparison was the drag on the aborted core stage during various launch abort scenarios predicted by a set of chemically reacting simulations that employ a 15-species,

30-reaction model developed by Niu *et al.*[9]

An overview of the simulation setup was provided, including the details of the numerical methods used and of the computational domain. The two-part solution procedure that saw the ACM and AM combustion chambers simulated separately from the full external flow over the SLS outer mold line was explained. These precursor simulations of the combustion chambers used the chemically reacting flow model. The state of the mixture at the ACM and AM nozzle outlets, including fluid dynamic properties and species mass fractions, was then used as an inflow boundary condition for the full simulations.

At the same time, the state of the gas at the nozzle outlets was used to develop a single equivalent species that provided identical values for ACM and AM thrust, temperature, and exit velocity. Combined with a single species for air in the freestream, 'equivalent' simulations of the full external flow and SLS abort scenarios that considered no chemical reactions were conducted. Additionally, for a selection of cases, these simulations were also conducted with calorically perfect air as the exhaust and freestream gases.

The axial force coefficient predicted by the two simplified models were compared to those obtained by the chemically reacting simulations. Overall, good agreement was observed between the equivalent species, perfect air, and chemically reacting models, with each model typically predicting CA to within 10% of each other. There were, however, instances where the combustion products would undergo additional heating after leaving the nozzle outlets as they crossed strong shocks. This was observed when the LAV traveled sufficiently far upstream and a strong bow shock was allowed to form on the leading edge of the aborted core stage. The plume gases were forced into the LAV wake by the freestream, and they impinged on the cavity at the leading edge of the aborted core stage after traveling through this shock and undergoing large increases in temperature. For the chemically reacting cases, this yielded changes in the composition of the exhaust gas mixture. The essentially 'frozen' exhaust gases used by the equivalent and perfect air models were unable to represent this change in composition, and large discrepancies in core stage CA were observed.

Finally, the cost comparison for each method was evaluated by advancing a given problem 20 Newton iterations and recording the wall-clock time that was required for each gas model. It was found that the chemically reacting cases are at least 4 times slower than the equivalent species and perfect air models, and required more memory to begin computation. The equivalent species model was only marginally slower than the perfect air model. It may be suggested then that in the creation of large databases considering powered launch vehicles, and depending on the quantity of interest, that all simulations should use a single equivalent species air model if available, and perfect air if necessary. This is of course only provided that: (1) reliable check cases can be run while considering chemically reactions at select locations in the database parameter space in order to ground the results obtained from the simple models and (2) the quantity of interest is largely pressure-driven, such as forces and moments. For the case of (significant) heating, as was shown in this paper, the equivalent species and perfect air models are incapable of representing the changes that the mixture of interest undergoes, and unsatisfactory results will be obtained.

Appendix

A. Evaluation of the Temperature Boundary Condition

All of the cases considered thus far have considered an adiabatic wall. Directly under the plumes and in regions around shocks and plume impingement, the wall could reach over one thousand Kelvin in temperature. This could drive additional reactions near the wall in the chemically reacting simulations. The external core stage, in practice, is coated with a material that would ablate as the temperature rose in an attempt to maintain a constant temperature, so a selection of the chemically reacting and equivalent species simulations were conducted again, this time modeling all surfaces of the launch vehicle as isothermal walls with $T_{wall} = 300K$. These results are briefly summarized in this appendix. It should be noted that the 'true' behavior of this ablative material is not described fully by an adiabatic or an isothermal wall boundary condition alone but some combination of the two, and the 'true' value of CA likely lies between the values obtained with each type of boundary condition.

Table 7 shows CA of the aborted core stage for the isothermal simulations as a percent change relative to the associated adiabatic case, both considering the chemically reacting exhaust gas model. The first observation is that all of the isothermal cases predict CA to within approximately 11% of those predicted by the adiabatic cases. The predictions of CA from the isothermal cases are higher than the adiabatic predictions, and for the application of this work, results in less conservative answers.

The most obvious effect of the temperature boundary condition is the temperature in the flow near the

Table 7: Summary of Core Stage Axial Force Coefficient for Isothermal Powered Simulations Using a Finite Rate Chemistry Model

$\Delta x/L_{ref.}$	Mach Number	AM Thrust	CA (relative)
0.5	0.7	Low	+1.88%
0.5	0.7	High	+5.79%
0.5	3.0	Low	+7.55%
0.5	3.0	High	+11.11%
1.5	3.0	Low	+8.48%
1.5	3.0	High	+10.17%
2.5	3.0	Low	-0.59%
2.5	3.0	High	11.30%

wall. Figs. 21a-21d show the temperature on a cut plane through the domain for two LAV offset distance simulations run with adiabatic and isothermal walls. The adiabatic cases show high temperature regions directly downstream of the LAV heat shield that are less pronounced in the isothermal cases. In addition, just past the leading edge of the aborted core stage, generally lower temperatures are observed for the cases considering the isothermal wall boundary condition. This effects the composition of the exhaust gas as additional reactions occur near the surface of the core stage, as is evident by contours plots of the mass fraction of H_2 near the body obtained with the isothermal wall. These plots can be directly compared to those in Fig. 22 that were obtained with the adiabatic wall. There are lower concentrations of H_2 near the leading edge of the core stage in the isothermal simulations.

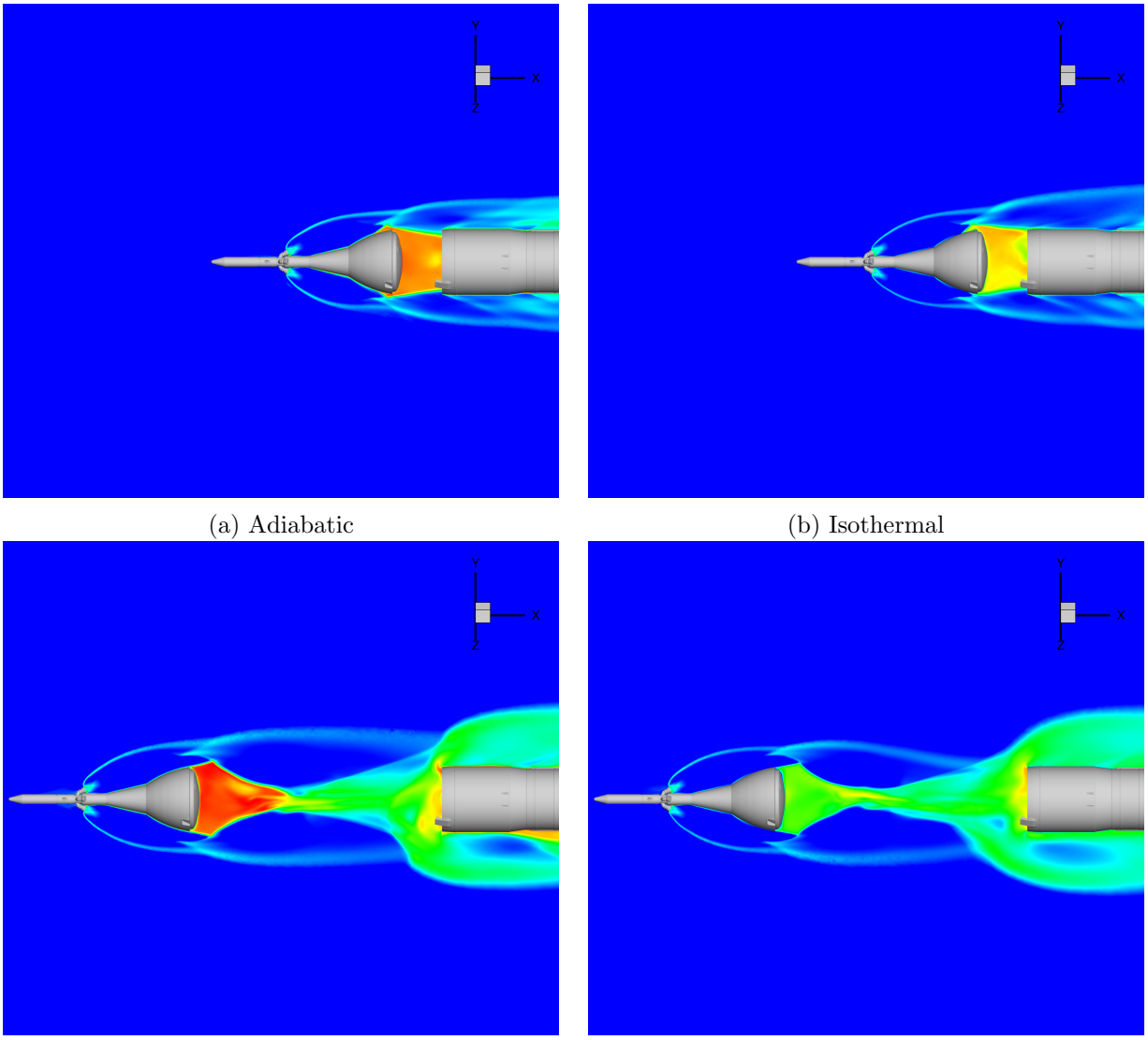

(a) Adiabatic

(b) Isothermal

(c) Adiabatic

(d) Isothermal

Figure 21: Saturated pseudocolor contours of temperature shown on a semi-transparent plane cutting the domain along the center-line of two AM nozzles for the (a)-(b) $M = 3.0$, $\Delta x.L_{ref.} = 0.5$, low-thrust and (c)-(d) $M = 3.0$, $\Delta x.L_{ref.} = 2.5$, high-thrust cases with adiabatic and isothermal walls.

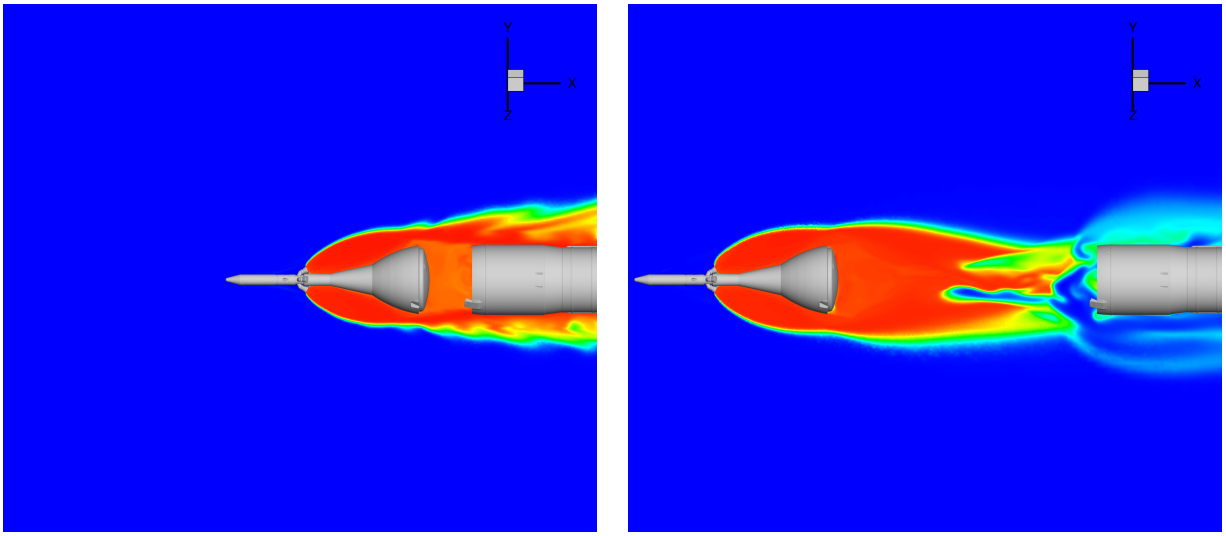

(a) $M = 3.0, \Delta x/L_{ref.} = 0.5$, low-thrust (b) $M = 3.0, \Delta x/L_{ref.} = 2.5$, high-thrust

Figure 22: (a)-(b) Saturated pseudocolor contours of the mass fraction of H_2 obtained by the chemically reacting simulations with an isothermal wall shown on a semi-transparent plane cutting the domain along the center-line of two AM nozzles.

B. Effect of Exhaust Gas Modeling on LAV Drag

Though not the primary focus of this paper, the drag and surface pressure on the departing LAV are of some interest. Prior internal work by NASA concluded that not properly modeling the correct chemical reactions, typically, under-predicting the number of species and reactions present, results in higher values of CA on the LAV. This is attributed to a variety of factors, most notably afterburning of the remaining SRM fuel mixture as the exhaust gases travel around the ogive and into the shear flow behind the LAV. The LAV drag and surface pressure are studied only superficially in this appendix in order to compare the current results qualitatively against these prior conclusions. Using the single equivalent species and perfect air exhaust gas models can be interpreted as under-predicting the number of species/reactions present in the flow field, and thus, we should expect to see larger values of CA for these cases.

Table 8 displays the predicted value of CA for the equivalent species and perfect air cases shown as a percent change relative to the associated case with the full finite rate chemistry model. As expected, CA is over-predicted for all cases using the simplified exhaust gas models. The over-prediction is significant for the cases using perfect air in the supersonic freestream conditions. The results from the subsonic case depicted in the first row show that both models overpredict CA by similar amounts compared to the chemically reacting model, and this is likely due to the AM plumes not impinging on the ogive of the LAV as they do in the cases at $M = 3.0$. Thus, any disagreement in plume strength and shape that occurs by using the perfect air model plays little effect on LAV CA at the subsonic freestream condition. At the LAV offset of $\Delta x/L_{ref.} = 2.5$, the differences are very small. This may be due to the fact that the LAV is clear of the recirculation bubble that forms between the heat shield and the leading edge of the core stage.

Table 8: Summary of LAV Axial Force Coefficient for Select Powered Simulations

$\Delta x/L_{ref.}$	Mach Number	AM Thrust	Equiv. Species CA (relative)	Perfect Air CA (relative)
0.5	0.7	Low	+17.43%	+17.00%
0.5	3.0	Low	+21.20%	+105.10%
1.5	3.0	Low	+9.92%	+153.85%
2.5	3.0	Low	+9.70%	+21.97%
2.5	3.0	High	+0.28%	+0.39%

In fact, with the equivalent species model, the two cases at $\Delta x/L_{ref.} = 0.5$ show the largest disagreement between CA and that predicted by the chemically reacting model. At this close LAV offset distance, there is a significant stagnated flow region between the heat shield on the LAV and the cavity of the aborted core stage. The temperature in this stagnated region is relatively large compared to the surrounding flow, and the gas may not be properly represented with the equivalent species model. This is also suggested by Figs. 16a and 21a, where large deviations from the exhaust gas mixture and high temperatures can be observed.

In the prior internal works by NASA, it was observed that under-resolving the number of species and reactions resulted in too low of a base pressure on the LAV. This may be the mechanism that drives CA to be over-predicted for these cases. Figs. 23a and 23b attempt to shed some light on this by extracting C_p along the length of the LAV for two LAV offsets. The results obtained by using all exhaust gas models are shown. Unfortunately, no strong conclusions can be made about the pressure on the base of the LAV, but some other interesting observations are immediately obvious. Differences primarily manifest in the location of the shock attachment points and the shock strengths. The largest differences occur just under the AM nozzles in Fig. 23b. This could be due to a number of factors including differences arising in the composition of the chemically reacting mixture that are not captured in the 'frozen' equivalent species or perfect air models. In regards to 'power-on' versus 'power-off', the primary effect of the plumes is the weakening of the strongest attached shock in the system that sits on the ogive of the LAV. This is due to the strong AM plumes weakening the downstream flow by strengthening the attached shock upstream of the AM nozzles.

Figs. 24a and 24b show the cumulative CA along the length of the LAV for the same cases, and much of the same conclusions can be observed here. Most notable of these is the large decrease in CA when the ACMs and AM are in the powered configuration, dramatically lowering the contribution to CA from the ogive of the LAV.

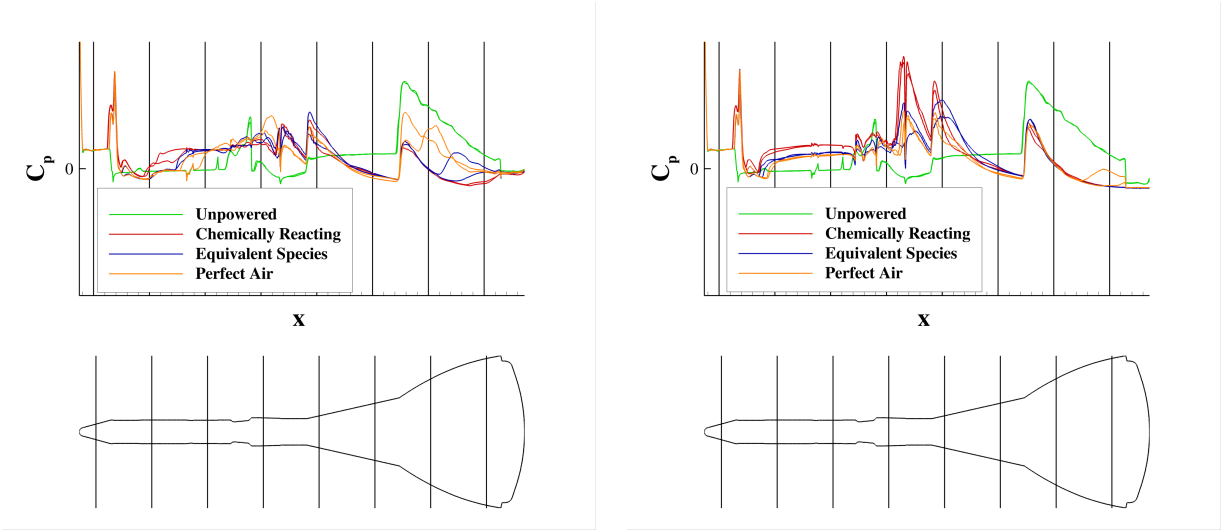

(a) $M = 3.0$, $\Delta x/L_{ref.} = 0.5$ (b) $M = 3.0$, $\Delta x/L_{ref.} = 2.5$

Figure 23: C_p extracted along a line defined by the $x - y$ plane and the surface of the LAV for the (a) low-thrust $M = 3.0$, $\Delta x/L_{ref.} = 0.5$ and (b) high-thrust $M = 3.0$, $\Delta x/L_{ref.} = 2.5$ cases using the different exhaust gas models.

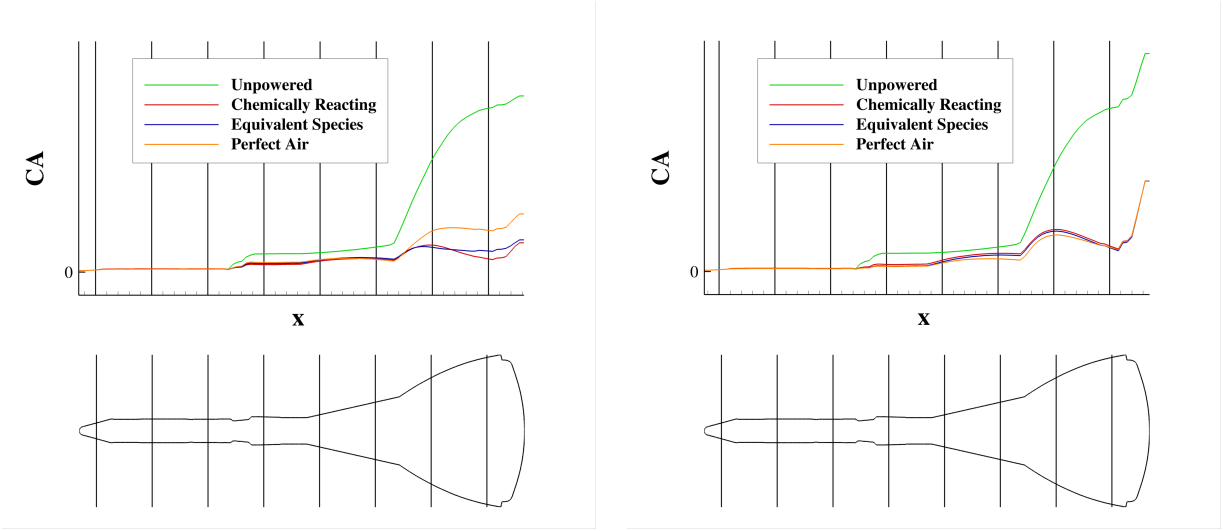

(a) $M = 3.0$, $\Delta x/L_{ref.} = 0.5$ (b) $M = 3.0$, $\Delta x/L_{ref.} = 2.5$

Figure 24: C_p extracted along a line defined by the $x - y$ plane and the surface of the LAV for the (a) low-thrust $M = 3.0$, $\Delta x/L_{ref.} = 0.5$ and (b) high-thrust $M = 3.0$, $\Delta x/L_{ref.} = 2.5$ cases using the different exhaust gas models.

Acknowledgments

The authors would like to thank Peter McCloud and Kirk Putnam from NASA Johnson Space Center for the 15-species, 30-reaction model used in this work for the attitude control and abort motor exhaust plumes. All simulations were conducted on NASA Advanced Supercomputing (NAS) systems at NASA Ames Research Center.

References

[1]Luke, E. A., Tong, X.-L., Wu, J., Cinnella, P., and Chamberlain, R., "Chem 2: A finite-rate viscous chemistry solver–the user guide," *Mississippi State University, Mississippi State, MS, Tech. Rep*, 2004.

[2]Luke, E. A. and George, T., "Loci: A rule-based framework for parallel multi-disciplinary simulation synthesis," *Journal of Functional Programming*, Vol. 15, No. 3, 2005, pp. 477–502.

[3]Applebaum, M., Eppard, W., and Hall, L., "Multi-Species Effects for Plume Modeling on Launch Vehicle Systems," *Journal of Spacecraft and Rockets*, Vol. 49, 09 2012, pp. 770–778.

[4]Marcum, D. L. and Weatherill, N. P., "Unstructured grid generation using iterative point insertion and local reconnection," *AIAA journal*, Vol. 33, No. 9, 1995, pp. 1619–1625.

[5]Marcum, D. L., "Unstructured grid generation using automatic point insertion and local reconnection," *The handbook of grid generation*, 1998, pp. 18–1.

[6]Venkatakrishnan, V., "Convergence to steady state solutions of the Euler equations on unstructured grids with limiters," *Journal of computational physics*, Vol. 118, No. 1, 1995, pp. 120–130.

[7]Wilcox, D. C., "Formulation of the kw turbulence model revisited," *AIAA journal*, Vol. 46, No. 11, 2008, pp. 2823–2838.

[8]Wilcox, D. C., "Dilatation-dissipation corrections for advanced turbulence models," *Aiaa Journal*, Vol. 30, No. 11, 1992, pp. 2639–2646.

[9]Qinglin, N., Zhihong, H., and Shikui, D., "IR radiation characteristics of rocket exhaust plumes under varying motor operating conditions," *Chinese Journal of Aeronautics*, Vol. 30, No. 3, 2017, pp. 1101–1114.

[10]McBride, B. J., *Coefficients for calculating thermodynamic and transport properties of individual species*, Vol. 4513, National Aeronautics and Space Administration, Office of Management, 1993.

[11]Meeroff, J., Lee, H. C., Dalle, D. J., Rogers, S. E., Roozeboom, N., and Baerny, J., "Comparison of SLS Sectional Loads from Pressure-Sensitive Paint and CFD," *AIAA Scitech 2019 Forum*, 2019.

[12]Dalle, D. J., Rogers, S. E., Lee, H. C., and Meeroff, J., "Adjustments and Uncertainty Quantification for SLS Aerodynamic Sectional Loads," *2018 Applied Aerodynamics Conference*, 2018, p. 3640.

[13]Abdol-Hamid, K. S., Ghaffari, F., and Parlette, E. B., "Ares I Vehicle Computed Turbulent Ascent Aerodynamic Data Development and Analysis," *Journal of Spacecraft and Rockets*, Vol. 49, No. 4, 2012, pp. 596–608.